ACS APPLIED ELECTRONIC MATERIALS

pubs.acs.org/acsaelm Article

Electrical, Magnetic, and Sensing Properties of Acetone in $Co_{3-x}Ni_xO_4$-rGO Samples

Leydi Julieta Cardenas F., Carlos Arturo Parra, Javier Alonso Cuervo F., Adenilson José Chiquito, Luis Carlos Moreno A., Julio Evelio Rodríguez, and Miryam Rincón Joya*

Cite This: https://doi.org/10.1021/acsaelm.4c00638 Read Online

ACCESS | Metrics & More | Article Recommendations

ABSTRACT: This study investigates the electrical, magnetic, and acetone detection properties of $Co_{3-x}Ni_xO_4$-rGO (cobalt−nickel oxide reduced with graphene) samples synthesized using two different methods: sol−gel and hydrothermal. The structure, morphology, electrical, and magnetic characteristics of the samples are examined, highlighting a significant change in those with 4% Ni and rGO addition via the sol−gel method. It is determined that the samples exhibit varistor and thermistor behavior, with nonlinear coefficients and variable threshold voltages. The inclusion of rGO positively affects the electrical properties by improving charge carrier mobility. Additionally, the samples' response to acetone as a target gas for vapor detection is investigated, observing significant changes in electrical resistance in its presence. Response times are short, with an acetone response R_g/R of 2.5 at room temperature and 1.1 at 200 °C, with the latter being the same sample that exhibited changes in magnetic properties. This study provides a detailed insight into the electrical, magnetic, and acetone detection properties of $Co_{3-x}Ni_xO_4$-rGO samples, highlighting the influence of the synthesis method on these properties and their potential for gas sensor applications.

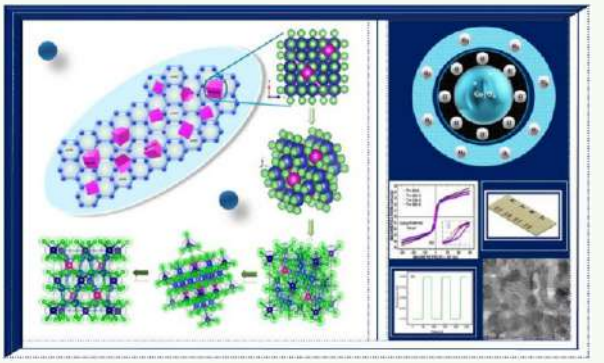

KEYWORDS: *Cobalt oxide, Magnetic, Sol−gel, Hydrothermal, Electrical properties, Sensing*

INTRODUCTION

Nanotechnology has brought about a new era of materials science with its ability to engineer and manipulate materials at the nanoscale. Among these materials, transition metal oxides such as cobalt oxide have gained significant attention due to their unique properties and potential applications in various fields such as catalysis,[1] energy storage, and sensing.[2] In recent years, efforts have been made to enhance the performance of these materials by introducing graphene-based composites. Graphene, with its high surface area and excellent electrical and thermal conductivity, has been shown to improve the electrical and magnetic properties of transition metal oxide composites.[3] The high electrical conductivity of graphene facilitates efficient electron transfer between the transition metal oxide and its surrounding environment.[4] This characteristic is especially crucial in sensor applications, where the detection of external signals heavily depends on the effectiveness of electron transfer mechanisms.[5]

Furthermore, the combination of graphene with transition metal oxides can result in unique structural and functional properties, making them ideal candidates for the development of high-performance devices.[6] The synthesis of these composites can be achieved through various methods, such as sol−gel[7] and hydrothermal techniques,[8] which can lead to different morphologies and properties. Additionally, the application of these composites in sensing devices has gained particular attention due to their high sensitivity and selectivity toward various gases and vapors.[9]

Gas sensing using reduced graphene oxide (rGO) has expanded beyond the use of transition metal oxides, and several other materials are commonly employed as composites with graphene for enhanced gas sensing properties, other metal oxides such as TiO_2, Fe_2O_3,[10] and CuO.[11] These findings provide valuable insights for the advancement of portable gas sensing devices with enhanced performance and the ability to detect commonly encountered organic vapors. Metal sulfides, such as CuS[11] and WS_2,[12] combined with rGO, offer increased sensitivity and selectivity toward various gases. In turn, metal−organic frameworks (MOFs) possess a large internal surface

Received: April 16, 2024
Revised: May 15, 2024
Accepted: May 17, 2024

area, allowing for high gas adsorption capacity;[13] when graphene is combined with MOFs, it forms a hybrid composite that combines the excellent electrical properties of graphene with the high gas sorption capabilities, resulting in improved gas sensing performance.[14] Additionally, composite structures have been created that offer enhanced gas sensing capabilities; also conductive polymers, such as polyaniline[15] and polypyrrole,[16] have attracted attention in gas sensing applications due to their tunable conductivity and chemical sensitivity. When graphene is combined with conducting polymers, it can enhance the overall electrical conductivity of the composite, leading to improved gas sensing performance and stability. The integration of metal nanoparticles, such as Au/SnO_2/rGO[17] and Ag/NiO/rGO,[18] in hybrid structures has led to the development of efficient sensors for ethanol and glucose detection. These hybrid structures offer a combination of high sensitivity, wide linear range, fast response time, and low interference,[19] making them suitable for various applications in the fields of environmental monitoring,[20] biomedical diagnostics,[21] and food industry quality control.[22]

The high surface area of rGO enables strong adsorption capabilities,[18] with abundant surface defects and functional groups providing sites for acetone molecules, leading to prolonged saturation and slower desorption. Evaluation of acetone sensors involves parameters such as response time, sensitivity, selectivity (ability to distinguish acetone from other gases), stability, and reproducibility. Various fabrication techniques, including sol−gel, hydrothermal synthesis, chemical vapor deposition, and electrodeposition, can be employed to fabricate $Co_{3-x}Ni_xO_4$-rGO sensors, influencing their structural properties, morphology, and performance. These sensors find applications in diverse fields, including electronic noses for metabolic disorder monitoring, industrial settings for detecting acetone emissions and ensuring workplace safety, and environmental monitoring to assess air quality and detect acetone pollution.[23]

P-type semiconductors are characterized by a predominance of positive charge carriers, known as "holes" in their conduction band. They exhibit different electronic properties compared to n-type semiconductors, where negative charge carriers (electrons) dominate. The gas sensing behavior of p-type oxide semiconductors is influenced by the interaction between the analyte gas and the surfaces of the semiconductor material.[24]

In the field of gas sensors, the morphology of nanostructures in p-type oxide semiconductors is crucial.[25] The size, shape, and arrangement of these nanostructures have a profound impact on gas accessibility and interparticle contacts, ultimately influencing the overall gas response. Smaller nanostructures are particularly advantageous for p-type oxide semiconductors as they offer a larger surface area, facilitating enhanced interaction with gas molecules and resulting in improved sensitivity.[26]

In this context, this study focuses on the synthesis, characterization, and evaluation of $Co_{3-x}Ni_xO_4$-rGO composites for their potential application in gas sensing. In this study, $Co_{3-x}Ni_xO_4$ with and without reduced graphene oxide (rGO) were synthesized using sol−gel and hydrothermal techniques. The resulting materials were characterized using various techniques such as electrical resistivity measurements, transmission electron microscopy (TEM), magnetic measurements, and gas sensing tests. The focus of this study was to investigate the influence of rGO on the morphology, magnetic, and electrical properties, and gas sensing performance of $Co_{3-x}Ni_xO_4$-rGO. Reduced graphene oxide (rGO) enhances the catalytic properties of porous Co_3O_4 by improving stability and increasing active site availability, while porous Ni-doped Co_3O_4 demonstrates efficiency in both oxygen evolution reaction (OER) and hydrogen evolution reaction (HER), particularly with low Ni doping concentrations like 4%.[27] The influence of Ni and rGO on Co_3O_4's properties impacts its structure, conductivity, and magnetic behavior, with successful Ni doping and 4% Ni doping creating small pores to provide more active sites. However, excessive Ni can hinder OER performance. Ni alters conductivity and magnetic coupling, while rGO enhances electrical and surface properties.

MATERIALS AND METHODS

The hydrothermal method began by dissolving cobalt acetate in distilled water, followed by the addition of nickel sulfate, urea, and 10 mg of rGO. The pH was adjusted by adding 2 mL of ammonia. The solution was then transferred to an autoclave and heated at 180 °C for 20 h. Subsequently, the resulting samples were washed with distilled water and ethanol, dried at 60 °C for 12 h, and calcined at 300 °C for 3 h. All samples underwent thermal treatment up to 850 °C. Next, acetone detection tests, known as sensing method 1, were conducted. For sensing method 2, the samples were pressed and exposed to a temperature of 1000 °C for 20 h before performing the acetone detection test.

The synthesis of $Co_{3-x}Ni_xO_4$ (x = 0.04) via sol−gel method employed cobalt nitrate hexahydrate ($Co(NO_3)_26H_2O$) and citric acid $C_6H_8O_7H_2O$ as precursors, with distilled water as the solvent. Initially, the solution was homogenized using magnetic stirring for 1 h at 60 °C. Subsequently, nickel nitrate hexahydrate $N_2NiO_6{\cdot}6H_2O$ was added in the specified percentages for this study with continuous stirring, along with 10 mg of rGO, resulting in two samples: one with rGO and another with only 4% Ni. Following this, the formed gel was dried for 4 h at 80 °C. Finally, the resulting product underwent thermal treatment in a Hobersal muffle furnace, reaching temperatures up to 850 °C.

The structural characterization of the samples was carried out using a PANalytical Xpert Pro X-ray diffractometer, applying the Bragg−Brentano configuration, with a gradual step of 0.02° in 2θ by t = 109 s, using a Cu Kα X-ray tube with λ = 1.5406 Å. The morphology and composition of the fibers were visualized on a scanning electron microscope (SEM, JEOL 6510). The Tecnai F20 Super Twin TMP transmission electron microscope (TEM), featuring a field emission source, offers a resolution of 0.1 nm at 200 kV, with a maximum TEM magnification of 1.0 million times (1.0 M×) and is equipped with a GATAN US 1000XP-P camera. It is employed for studying the internal structure of materials, delivering detailed images of particle morphology and size at the nanoscale. The VSM-VersaLab Quantum Design operates between 50 and 300 K with magnetic fields up to 30 kOe. It characterizes and comprehends material magnetic properties, such as saturation magnetization, essential for evaluating their magnetic field generation capability. Furthermore, it analyzes magnetic hysteresis, unveiling properties like coercivity and remanence. It is instrumental in characterizing magnetic materials, including permanent magnets and various ferromagnetic, ferrimagnetic, or antiferromagnetic types. Measurements using instruments such as the Keithley Nanovoltmeter model 2182A and an AC−DC current source model 6221 are conducted to characterize the electrical properties of materials. These measurements are crucial for comprehending how materials react to the application of electrical current and voltage under various conditions.

SENSOR DEVELOPMENT

Method 1. Samples of $Co_{3-x}Ni_xO_4$ and $Co_{3-x}Ni_xO_4$-rGO synthesized by sol−gel and hydrothermal[28] techniques were mixed with isopropyl alcohol to produce pastes that were

https://doi.org/10.1021/acsaelm.4c00638
ACS Appl. Electron. Mater. XXXX, XXX, XXX−XXX

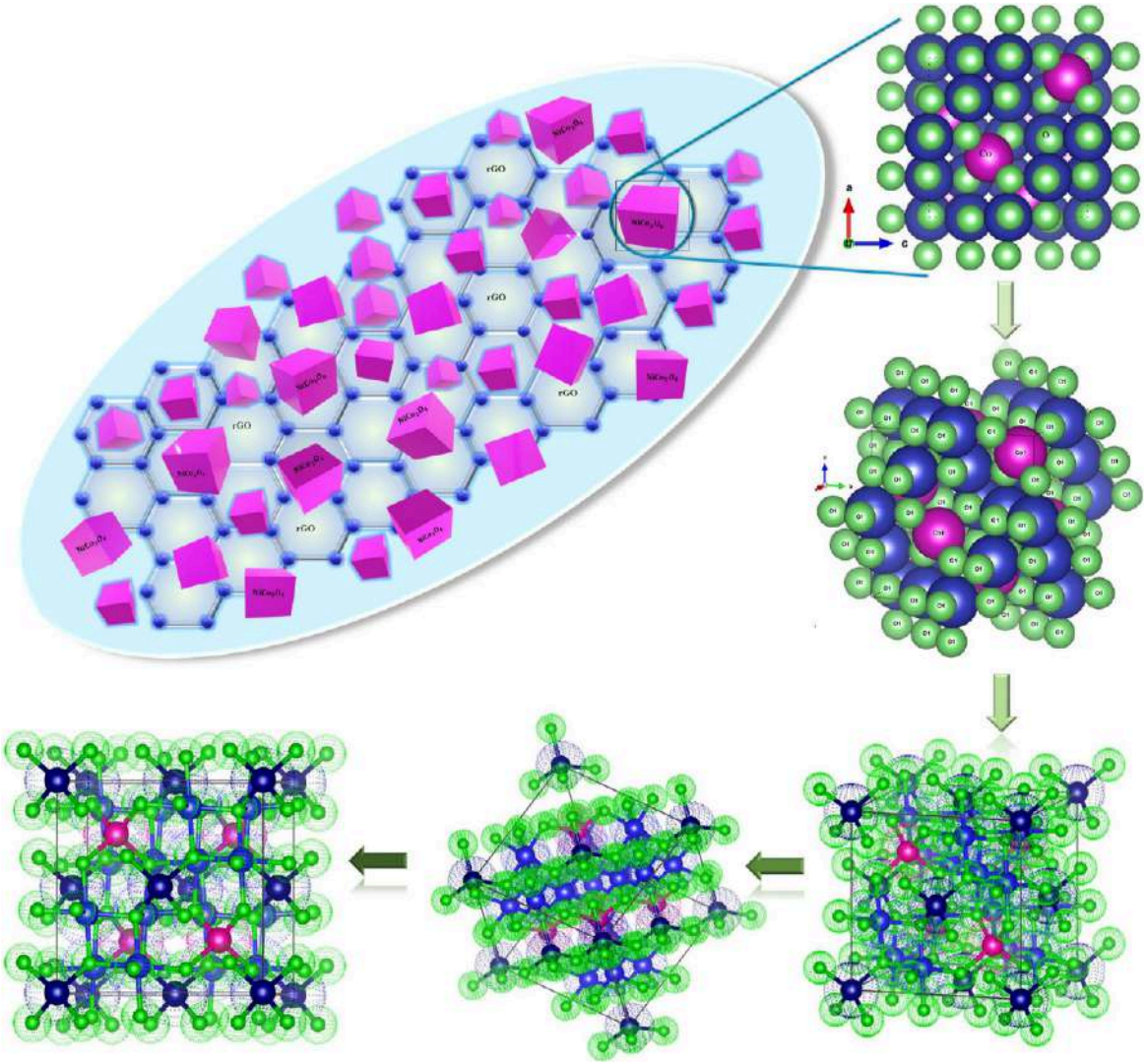

Figure 1. Schematic distribution of $Co_{3-x}Ni_xO_4$-rGO by the hydrothermal technique.

uniformly coated on a flat ceramic surface; then two copper contacts were soldered. The configuration for application consists of a gas chamber in which the sensing element is fixed; the variations in electrical resistance with respect to the analyzed gases were monitored by means of an electrometer. Gas vapors corresponding to methanol, ethanol, and acetone were injected with a flow rate of 50 sccm and an estimated concentration of 1000 ppm at room temperature, emitting results associated with each injection pulse, which were monitored through the computer. It is necessary to clarify that all measurements were at room temeperature.

The sensors, fabricated using $Co_{3-x}Ni_xO_4$-rGO obtained through sol−gel and hydrothermal techniques (method 1), were subjected to exposure of methanol (CH_3OH), ethanol (C_2H_5OH), and acetone (C_3H_6O) vapors at room temperature. The concentrations of these vapors ranged from 10 to 1000 ppm. Each sensor was exposed to the vapor for 10 s, followed by a 10 s recovery time.

Method 2. The samples were ground in an agate mortar. The powders were pressed under 400 and 1000 atm. They were then sintered at 1000 °C for 24 h in a Heraus furnace. The samples were prepared following the same procedure as in method 1 and subsequently underwent another sintering process at 1000 °C. Ceramic samples or pellets with copper wire contacts were fixed on the samples and placed on a ceramic plate to facilitate resistance measurements and to evaluate their behavior to acetone vapor.

Graphene supported on Co_3O_4 has demonstrated considerable potential in diverse applications, owing to the synergistic effects of its constituent elements. Nonetheless, the full extent of its potential applications remains to be thoroughly explored and communicated within the scientific community. A critical aspect of this system lies in the surface area and electrical conductivity of graphene, which play pivotal roles in determining the transformation and properties of the $Co_{3-x}Ni_xO_4$-rGO composite. Figure 1 depicts a schematic representation of this composite material, comprising $Co_{3-x}Ni_xO_4$ and reduced graphene oxide (rGO), highlighting the intricate synergy between the components at the nanoscale level. This synergy holds the promise of conferring distinctive properties upon the composite material, thereby opening up avenues for its utilization across a spectrum of technological applications. Moreover, the rGO is intricately supported on the surface of $Co_{3-x}Ni_xO_4$, contributing to the specific functional[29] catalytic, electric, and magnetic properties exhibited by the composite material.

https://doi.org/10.1021/acsaelm.4c00638
ACS Appl. Electron. Mater. XXXX, XXX, XXX−XXX

RESULTS AND DISCUSSION

The XRD patterns of the annealed samples (pressed pellets) used for gas sensing are shown in the Figure 2. As an illustrative example, we present here the XRD pattern of the sol−gel sample with 4% Ni and the addition of rGO. The diffraction patterns for the other annealed samples were similar. For the nonannealed samples, the corresponding diffraction patterns can be found in another publication.[28]

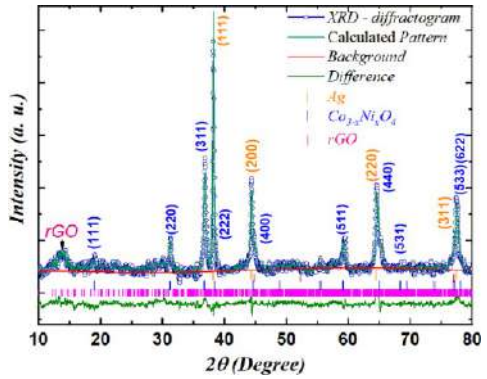

Figure 2. Rietveld refinement employed to analyze the crystalline structure of $Co_{3-x}Ni_xO_4$-rGO, in the sample synthesized via the sol−gel method and subjected to a sintering process at 1000 °C for 24 h (method 2).

Both the annealed samples for the sensing pellets and the nonannealed samples exhibit diffraction peaks indicative of the spinel structure of Co_3O_4. Additionally, Figure 2 illustrates the diffraction peaks of silver, which was employed to create electrical contacts in the pellet used for the sensing experiments. It is worth noting that these measurements were taken after the sensing analysis, hence the presence of silver peaks traces. Furthermore, the intensity of the (222) peak appears enhanced, possibly due to its overlapping with the silver peak (111). The XRD pattern in Figure 2 corresponds to the face-centered cubic phase of the Co_3O_4 spinel (Reference Code 04-021-8094) for the analyzed sample. The identified (hkl) planes and their corresponding 2θ values are as follows: (220) with 2θ = 31.3, (311) 2θ = 36.8, (222) 2θ = 38.5, (400)2θ = 44.8, (511) 2θ = 59.3, (440)2θ = 65.2, (533)2θ = 77.3, and (622)2θ = 78.4. The crystal size of $Co_{3-x}Ni_xO_4$ ($Co_{2.88}Ni_{0.12}O_4$) along the (311) plane was determined using the Scherrer equation, resulting in a value of 65.4 nm. Upon comparing the obtained crystal size value with the literature value for Co_3O_4 doped with 4% Ni,[28] a slight increase in size is observed. This could be attributed to the higher temperature during the recalcination process at 1000 °C of the sample in Figure 2.

From $Co_{3-x}Ni_xO_4$ (x = 0.12), we can state the following: Rietveld refinement of the XRD patterns was analyzed using the GSAS software code, with the ICDD PDF file 04-021-8094 and COD database code 9005887 as reference, resulting in a cubic spinel structure with space group $Fd\bar{3}\,m$ (227), achieving

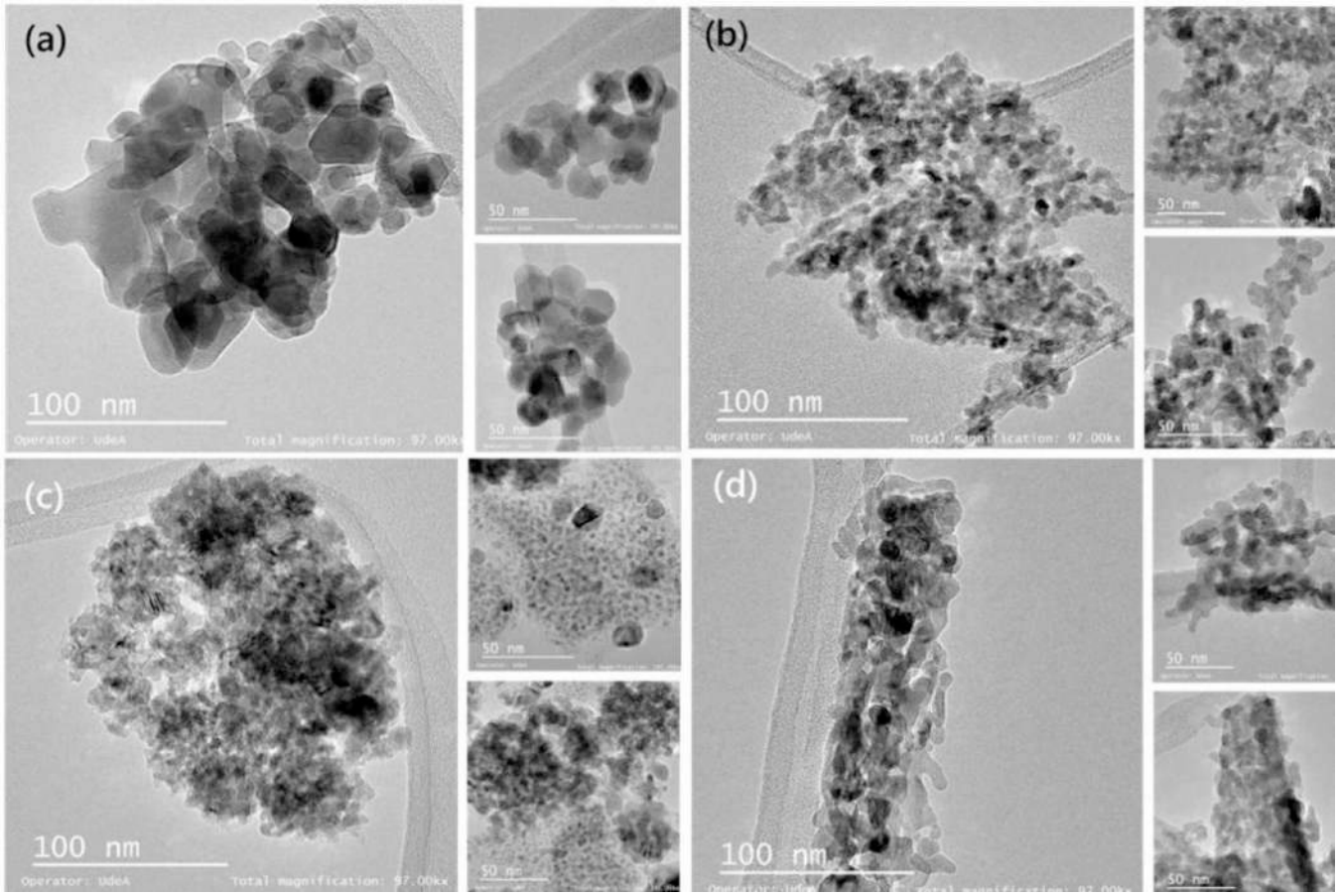

Figure 3. TEM micrographs of $Co_{3-x}Ni_xO_4$ samples: (a) 4% Ni sol−gel; (b) 4% Ni hydrothermal; (c) 4% Ni + rGO sol−gel; and (d) 4% Ni + rGO hydrothermal, method 1.

https://doi.org/10.1021/acsaelm.4c00638
ACS Appl. Electron. Mater. XXXX, XXX, XXX−XXX

a good fit. The calculated lattice parameter value was $a = b = c = 8.1062(15)$ Å, with a unit cell volume of 532.66 Å^3. The rGO was fitted considering the COD database code 2228856 of the $C_{108}H_{136}O_{20}$ structure with monoclinic space group $P1_21_1$ (4), yielding calculated lattice parameters of $a = 8.6662(3)$ Å, $b = 12.7310(2)$ Å, $c = 29.7058(3)$ Å, and a unit cell volume of 1410.81 Å^3. As the final phase in the refinement, the remainder of the silver electrodes was considered, Ag_4, with COD database code: 9011607, exhibiting lattice parameters of a = b = c = 4.0869(6) Å and a unit cell volume of 68.26 Å^3. The refinement confidence factors demonstrate a good fit for all three phases as follows: $\chi^2 = 4.15$, $R(F^2) = 7.32\%$, $R_p = 4.31\%$, and $R_{wp} = 3.91\%$ in Figure 2.

Figure 3 shows the TEM micrographs of the $Co_{3-x}Ni_xO_4$ and $Co_{3-x}Ni_xO_4$-rGO samples obtained by hydrothermal and sol−gel techniques. In this case, the samples were not annealed at 1000 °C and were used for sensing method 1. The well synthesized nanocrystals have crystalline, sharp, exposed and regular faces as observed in (a), (b), (c), and (d). The nanocrystals exhibit well-defined crystalline structures with sharp and regular faces, indicating a controlled growth process and high structural integrity. High pressure of water during hydrothermal synthesis likely creates pore spaces within the nanocrystal structure, resulting in the formation of nanostructures. Boundary layers between adjacent crystalline planes suggest interactions that give rise to defects and grain boundaries in the tight junction regions surrounding the pores.[30] These features have implications for gas sensing applications as defects can serve as active sites for chemical reactions and provide increased surface area for gas adsorption.[31] The presence of pore spaces within the nanostructures facilitates efficient gas adsorption and interaction with the sensing material, enhancing gas sensing performance in terms of sensitivity and response times.[32]

The synthesis method, whether hydrothermal or sol−gel, significantly impacts the particle size distribution and its relationship with the sensing properties of $Co_{3-x}Ni_xO_4$-rGO nanostructures. Factors such as temperature, pressure, reaction rate, precursor concentration, and synthesis duration are crucial in shaping these nanostructures, affecting particle nucleation, growth, and agglomeration, thereby determining their size distribution. Additionally, variations in synthesis conditions can result in different crystalline structures, morphologies, and surface properties, further impacting the detection capabilities of the nanostructures. While Figure 3 a and b) show larger particle sizes for the sol−gel method, opposite trends are observed in Figure 3 c and d). In the case of hydrothermal synthesis with the addition of rGO in this study, there is a possibility that reduced graphene oxide may be washed away during sample cleaning due to its tendency to remain on the surface throughout the process, unlike in the sol−gel method. Therefore, the synthesis approach significantly contributes to achieving the desired material properties. Moreover, particle size influences the surface area of the nanostructures, affecting their ability to detect gases.[33] A larger surface area provides more active sites for gas adsorption, thereby improving the material's sensitivity to gas presence. Consequently, a smaller particle size generally correlates with a larger surface area and, therefore, better gas detection capability in the nanostructures.

The 4% Ni compound was selected for characterization following previous investigations conducted by the group, which encompassed TEM and Raman analysis across various Ni concentrations (0% to 16%), as well as the effects of calcination temperature on the samples.[34,35] Within this range, the 4% Ni compound exhibited the most promising characteristics and surface area, thereby justifying a comprehensive analysis of its electrical, magnetic, and sensing properties.

The morphology depicted in Figure 4a corresponds to the pellet sample that underwent a second round of calcination

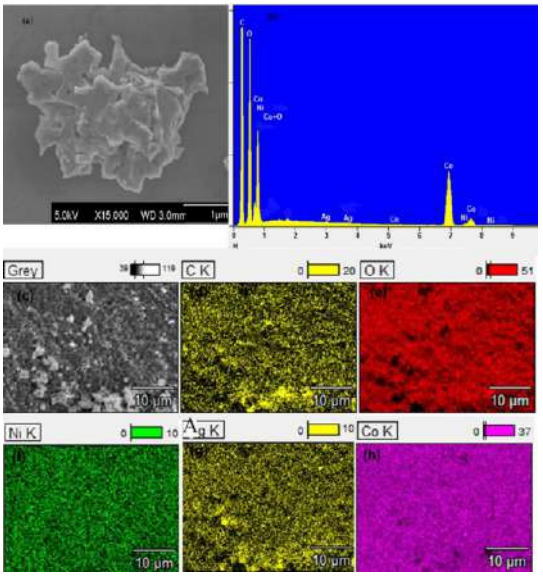

Figure 4. $Co_{3-x}Ni_xO_4$-rGO: (a) FESEM (field-emission scanning electron microscopy) image of the pellet samples synthesized via the sol−gel method, subjected to a sintering process at 1000 °C for 24 h. (b−h) Element detection by energy-dispersive spectroscopy (EDS) in SEM (scanning electron microscopy).

and pressing using method 2. This process transformed the sample into the spinel phase, subjecting it to a temperature of 1000 °C for 24 h to produce robust sintered samples, facilitating their manipulation for the placement of electrical contacts. As illustrated in the figure, the morphology of the sol−gel sample is characterized by the presence of large grain clusters, similar to the results obtained for the hydrothermal sample. Therefore, we will only present the sol−gel sample as an example in Figure 4.

It is crucial to elucidate the methodology employed for compositional analysis, particularly regarding the data showcased in Figure 4. Energy Dispersive Spectroscopy (EDS) analysis was utilized to validate the presence of expected chemical constituents, namely Co, Ni, O, and C, in the proportions depicted. However, it is essential to note that the values obtained via EDS analysis may vary due to factors such as the region of sample analysis and other experimental conditions. Therefore, it is pertinent to clarify that these values are approximate and do not represent absolute figures. Furthermore, it is emphasized that the primary objective of this analysis is to identify the presence of specific elements rather than precisely quantify their amounts. The sample represents the 4% Ni + rGO in the synthesis process, and similar results were obtained for the remaining samples. Hence, our aim was to ascertain the presence of the chemical elements C, Co, Ni, and Ag without quantifying them.

Magnetic Characterization. Figure 5 exhibit the diverse range of magnetic behaviors observed in materials such as Co_3O_4, Ni, and other dopants, spanning from ferromagnetic to

https://doi.org/10.1021/acsaelm.4c00638
ACS Appl. Electron. Mater. XXXX, XXX, XXX−XXX

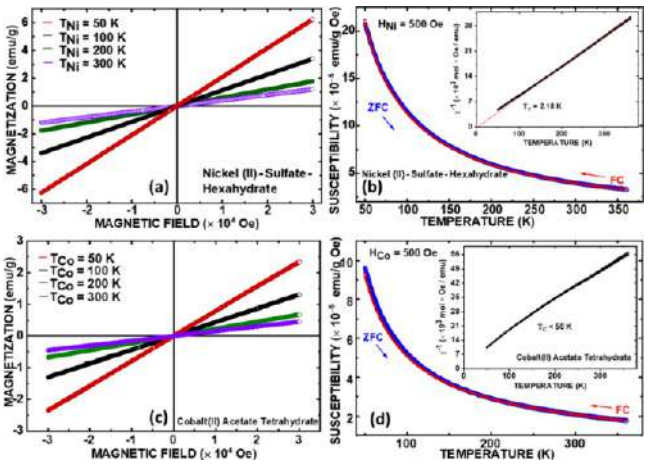

Figure 5. Magnetic behavior of the precursor samples (a, b) Ni and (c, d) Co.

antiferromagnetic at low temperatures. A detailed analysis of the magnetization **M** of the samples (Ni) and (Co) was conducted using (**H**) curves of magnetic nanoparticles, revealing a significant influence of temperature (T) on magnetic behavior, characterized by a gradual decrease in magnetization as T increases.[36,37]

The Curie temperature (T_c) recorded below 50 K for the precursors can be attributed to a variety of factors, including material composition, crystalline defects, particle size, and their interactions. To enhance T_c, optimization of material composition, crystalline purity, control of particle size, and morphology, as well as exploration of different synthesis techniques or post-treatments are proposed to promote more coherent magnetic behavior and increase magnetic ordering efficiency.[38]

Panels a and c of Figure 6 depict magnetic isotherms of commercially obtained Co_3O_4 samples and $Co_{3-x}Ni_xO_4$ samples prepared via hydrothermal methods, respectively, both exhibiting paramagnetic behaviors. In Figures 6b) and 6d), susceptibility is illustrated as a function of temperature, revealing a ferri−antiferromagnetic transition around 190 K in Figure 6b), with a negative constant upon linearization of the graph. Conversely, Figure 6d) shows a pattern of antiferromagnetic linearization in inverse susceptibility.[39]

In reference to Figure 6, the sample stands out for displaying a coupled magnetic response due to its nonmonophasic nature. During certain temperature intervals, these phase transitions become more apparent, showcasing different ferri and antiferro behaviors.[40] Although the antiferro phase may predominate, the ferrimagnetic transition between 50 and 100 K can induce notable changes in the curvature of the magnetic response. These changes arise from interactions among the various magnetic phases present, contributing to the observed magnetic complexity in the sample. Additionally, variations in curvature suggest a magnetic anisotropy that varies with temperature,[41] confirmed by analyzing the first derivative of susceptibility.[42] Although no significant changes are observed in this phase transition, a slight deviation in the curve is evident, supported by a background indicating contributions from different magnetic phases. It is crucial to recognize that this ferro-antiferro process can be influenced by various factors, such as sample composition and synthesis conditions, emphasizing the need for detailed investigations in future studies.

The ferro−antiferro transition in an oxide like Co_3O_4, whether pure or doped with Ni, arises from a combination of factors.[42] Ni doping introduces defects into the crystal lattice of Co_3O_4,[43] disrupting the configuration of cobalt atoms and their magnetic interaction,[44] leading to a competition between ferromagnetic and antiferromagnetic interactions in the

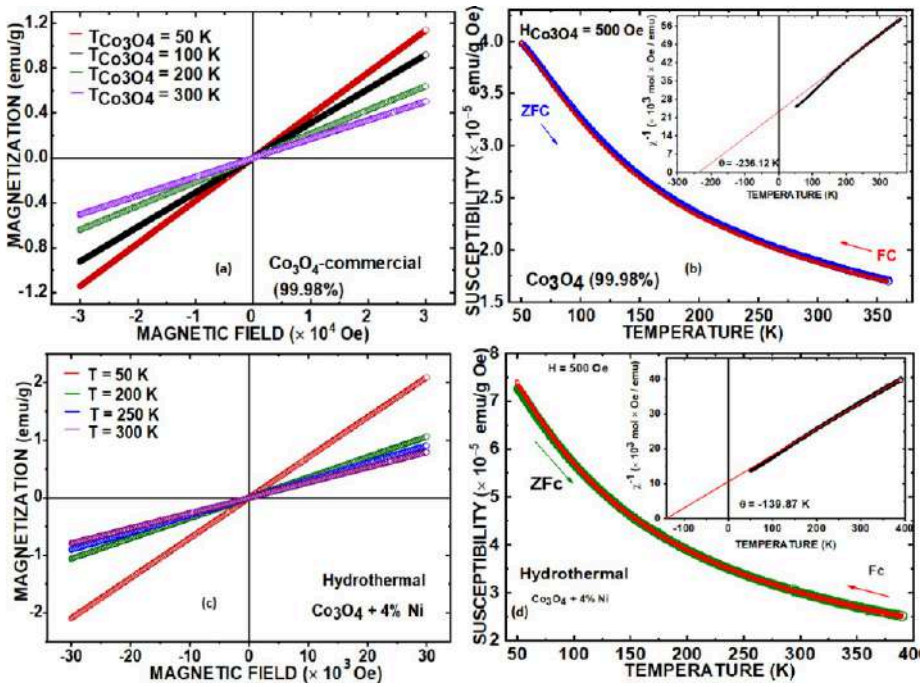

Figure 6. Magnetization isotherms measured from 50 to 300 K for Co_3O_4 (a, b) commercial and (c, d) for ($Co_{3-x}Ni_xO_4$, $x = 4$) by hydrothermal synthesis.

https://doi.org/10.1021/acsaelm.4c00638
ACS Appl. Electron. Mater. XXXX, XXX, XXX−XXX

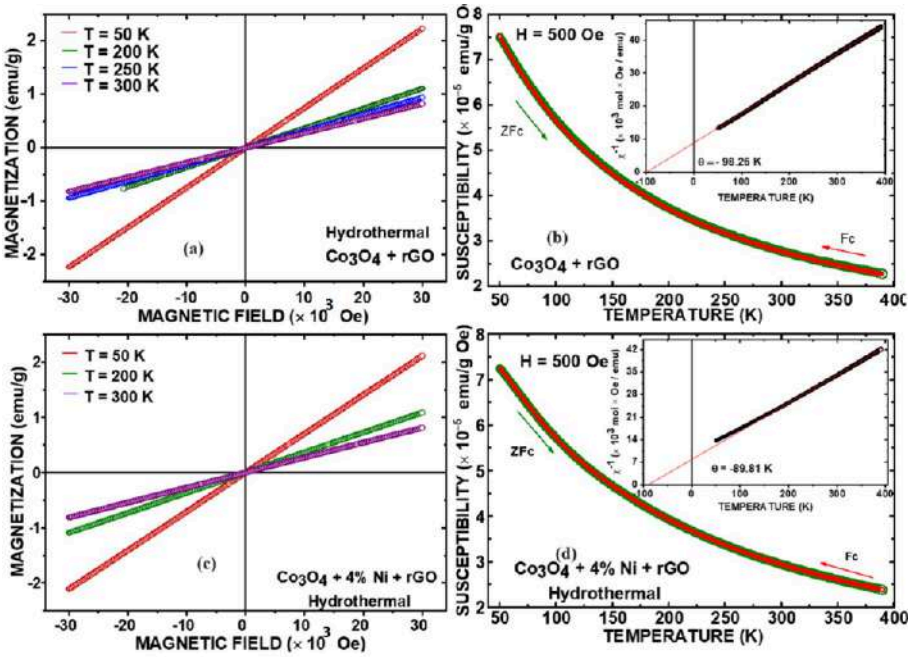

Figure 7. M vs H for the samples Co_3O_4-rGo: (a, c) $Co_{3-x}Ni_xO_4$-rGO, susceptibility for H 500 Oe vs temperature; (b) Co_3O_4-rGo and (d) $Co_{3-x}Ni_xO_4$-rGO by the hydrothermal method.

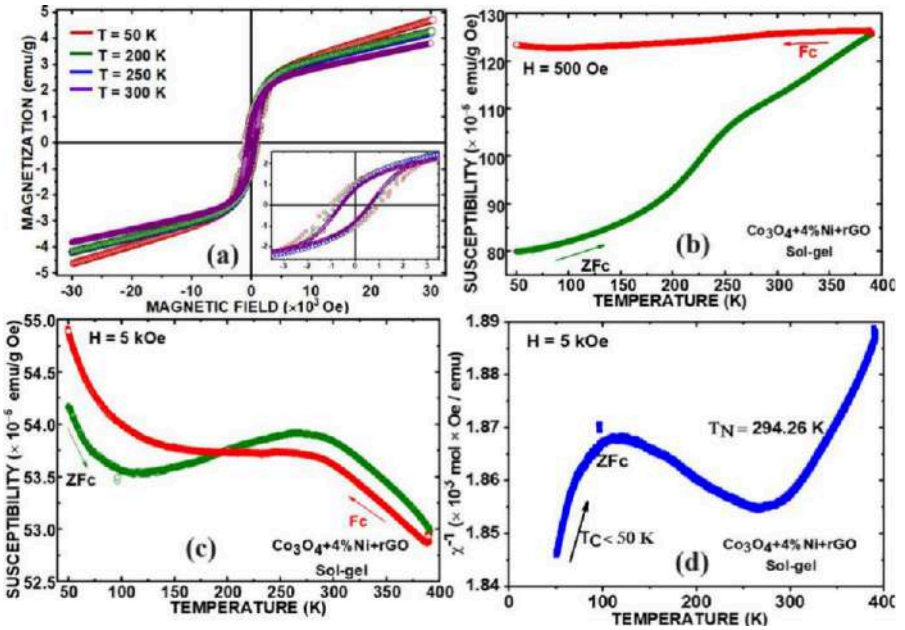

Figure 8. $Co_{3-x}Ni_xO_4$-rGO sample prepared using the sol−gel method was studied with the following measurements: (a) Magnetization (M) vs magnetic field (H), (b) susceptibility as a function of temperature for a magnetic field strength of 500 Oe, (c) susceptibility vs temperature for a magnetic field strength of 5 kOe, and (d) inverse of susceptibility as a function of temperature for a magnetic field strength of 5 kOe.

material. Additionally, Ni doping can alter the density of electronic states near the Fermi level, affecting the band structure and stability of different magnetic states.[45] These changes can result in a reorganization of magnetic moments and a change in the magnetic orientation of the material. Defects introduced by Ni doping can also serve as anchoring centers for magnetic moments, favoring certain magnetic configurations over others at specific temperatures. Collectively, these effects can lead to the observation of a ferro-antiferro transition as temperature varies or other experimental conditions are modified. The ferro−antiferro transition in Co_3O_4, whether pure or doped with Ni, is the result of a

https://doi.org/10.1021/acsaelm.4c00638
ACS Appl. Electron. Mater. XXXX, XXX, XXX−XXX

complex interaction between defects, changes in band structure, and redistribution of magnetic moments. Fully understanding this phenomenon requires a comprehensive analysis combining both experimental and theoretical approaches to the magnetic properties of the material.

In Figure 7 a) and 7 c), the plots of **M** (magnetization) and **H** (magnetic field) for the samples obtained through the hydrothermal method, namely Co_3O_4-rGO and $Co_{3-x}Ni_xO_4$-rGO, exhibit a paramagnetic behavior.

This indicates the absence of magnetic disorder in the samples. Moving on to graphs 7 b) and d), the plots depict the susceptibility as a function of temperature for a magnetic field strength of 500 Oe. The insets display the inverse of the susceptibility, revealing an antiferromagnetic behavior for both samples. The only difference lies in the value of the Weiss constant, θ. The magnetic transition temperature (TN) of a sample, such as Ni-doped Co_3O_4, can be influenced by various factors, including chemical composition, microstructure, surface effects, processing conditions, and interactions between cobalt and nickel atoms. . It is essential to consider these factors when interpreting the TN of a specific sample. The provided TN temperature offers an approximate estimation and may not accurately represent the true Néel temperature due to the nonmonophasic nature of the samples and the potential influence of magnetic irregularities,[46] including those arising from secondary phases or the presence of a metastable state. Furthermore, if $\theta$is negative, indicating a transition to a paramagnetic state above the critical temperature (θ), the material is expected to exhibit paramagnetic behavior.

Figure 8 presents the magnetic measurements results for the sample obtained through the sol−gel method. In contrast to the samples obtained through the hydrothermal method, this sample exhibits distinct magnetic behavior. In Figure 8a), the isotherms display a hysteresis curve, indicating nonhomogeneous magnetic behavior. The dominant contribution observed in the M vs H isotherms corresponds to ferromagnetic behavior, particularly at magnetic fields above 500 Oe. In ferromagnetic materials, the magnetic moments of atoms align in the same direction due to strong magnetic interactions, resulting in high magnetization in the presence of an external magnetic field. However, there is also an antiferromagnetic contribution evident in the apparent nonsaturation of the isotherms, characterized by lines with a positive slope, observed above approximately 2500 Oe. The hysteresis curve of the $Co_{3-x}Ni_xO_4$-rGO nanoparticles at 50 K shows a ferromagnetic behavior with a saturation magnetization of 3.5 emu·g^{-1} at the maximum field of 30 kOe, while the hysteresis curve for the samples at 300 K shows an aproximate saturation magnetization value of 2.5 emu·g^{-1} in the applied field of 30 kOe, respectively. In the inset of Figure 8, it appears that there is a remnant magnetization that adds to the existing magnetization due to the material's composition. There is a relationship between the coercive magnetic field and the increase in remnant magnetization. In Figure 8a), the coercive field (HC) is depicted as a function of temperature, revealing values of 570 Oe at 300 K and 909 Oe at 50 K. Moreover, the remaining magnetization at 50 K is 1.13 emu·g^{-1}, whereas at 300 K, it measures 0.78 emu.

The relationship between the composition of a material and its remnant magnetization is crucial for understanding its magnetic behavior. This relationship may be more influenced by the material's granularity than by its inherent properties. For example, in antiferromagnetism, where magnetic permeability is low, a reduction in remnant magnetization is observed, as evidenced by the small slope of the $M(H)$ curve. This is explained by the intrinsic magnetic properties of the constituent elements and their arrangement within the material's structure.

Remnant magnetization, also known as residual magnetization, represents the residual magnetic field that remains in the material after removing the external magnetic field. Factors such as the magnetic moments of the constituent elements, the crystal structure, and the presence of impurities or defects can influence the amount of remnant magnetization exhibited by a material. For example, materials composed of elements with strong magnetic moments, such as iron, nickel, and cobalt, tend to exhibit higher remnant magnetization.

On the other hand, the zero field cooling (ZFC) technique provides a comprehensive view of the material's magnetic response. During ZFC, the sample is cooled from a higher temperature to a lower temperature without the presence of an external magnetic field. This process allows thermally activated magnetic domains to freeze as the temperature decreases, resulting in an increase in magnetic susceptibility. The ZFC curve reveals the contribution of these thermally activated magnetic domains to the overall magnetic response of the sample, thereby providing valuable information about its magnetic behavior and the interactions between magnetic domains. In Figure 8b, the ZFC response represents the net response of the sample, while the FC (field cooling) response encompasses the sum of all possible contributions.

Figure 8 c illustrates the behavior of FC susceptibility at an applied magnetic field of 5 kOe, where alignment of magnetic domains with the field leads to a rapid increase in magnetization. Conversely, in ZFC, the material's magnetic anisotropy can result in slower growth or even a decrease in magnetization and susceptibility at lower temperatures, as observed at 100 K. As temperature increases, a crossover temperature is reached where FC and ZFC curves intersect, typically around 196 K. This intersection may stem from changes in magnetic interactions within the material, reflecting forces between the magnetic moments of atoms or ions classified as ferromagnetic, antiferromagnetic, or ferrimagnetic. Energy barriers also play a role, with higher barriers indicating greater resistance to changes in magnetic orientation, resulting in higher coercivity. The alignment of magnetic domains, where moments align, contributes to the observed magnetization. In Figure 8 d, the inverse susceptibility plot at a 5 kOe magnetic field exhibits three distinct contributions. At the Neel temperature of 294.26 K, an antiferromagnetic contribution emerges, marking a transition from paramagnetic to antiferromagnetic known as the ferro−antiferro compensation temperature. This transition arises from multiple crystalline phases, particularly para-ferro and para-antiferro, with the para-antiferro phase apparent below 294.26 K, exhibiting antiferromagnetic behavior characterized by the alignment opposite of magnetic moments.[47]

Second, at temperatures below 50 K, a ferrimagnetic Curie temperature is observed. At this point, the material undergoes a transition where the magnetic moments align in a ferrimagnetic configuration due to Co,Figure 5d. This configuration results in a net magnetization due to the combination of magnetic moments with opposing directions but different magnitudes. Lastly, along the curvature of the curve, a ferromagnetic behavior governs. This indicates that, at intermediate temperatures, the material exhibits ferromagnetic

https://doi.org/10.1021/acsaelm.4c00638
ACS Appl. Electron. Mater. XXXX, XXX, XXX−XXX

properties with a dominant alignment of magnetic moments in the same direction. It is also possible that there are additional contributions from magnetocrystalline anomalies, which can further influence the magnetic response of the material. Alberto et al.[48] reported that precise control of the site occupancy of $Co^{2+,3+}$, and $Ni^{2+,3+}$ ions can lead to a significant enhancement in net magnetization.[49] Octahedral Co^{3+} ions have a d^6 configuration in a low-spin state, while tetrahedral Co^{2+} ions have a d^7 configuration in a high-spin state.[50] The contribution of cobalt, nickel, and oxygen ions to the magnetization of the lattice relies on their oxidation states and their interaction within the crystalline structure. Typically, the presence of Co^{2+} and Ni^{2+} ions enhances the material's magnetization, while the influence of oxygen is more closely tied to its arrangement within the crystal lattice and its interaction with metallic ions.The observed effect can be attributed to the synthesis method utilized, which allows for better control over the site occupancy of these ions, unlike the hydrothermal method.[48]

Theoretical and experimental research[51] has shown that introducing oxygen and cation vacancies effectively triggers ferromagnetism in materials. In these compounds, Co^{3+} ions occupy octahedral sites (B), while Co^{2+} ions occupy tetrahedral sites (A), leading to a pairing of all d electrons of Co^{3+} and resulting in no overall magnetic moment. Spinel oxides, characterized by complex electronic interactions among spin, orbital, and charge degrees of freedom, demonstrate a close relationship between oxygen vacancies and spin structure due to superexchange interactions.[52]

Previous studies using first-principles methods have predicted the onset of ferromagnetism in Co_3O_4, with oxygen vacancies influencing the spin states significantly.[48,51,52] Calculations revealed that normal Co_3O_4 lacks a net magnetic moment, but the presence of oxygen vacancies leads to a measurable total magnetic moment. Specifically, CoB ions in oxygen-free Co_3O_4 exhibit zero magnetic moment, whereas those with oxygen vacancies show nonzero values. Moreover, the magnetic moments of oxygen ions bonded to CoB ions also undergo changes. Spin splitting, elucidated through density of states analysis, primarily arises from specific orbitals of CoB and CoA ions, as well as oxygen ions. Previous research has associated ferromagnetism in Co_3O_4 with uncompensated spins on its surface, suggesting a similar mechanism for observed ferromagnetism and highlighting the likely contribution of oxygen vacancies.[48,52]

The introduction of oxygen and cation vacancies in materials, especially in spinel oxides, significantly alters spin states, particularly in Co_3O_4, where they induce measurable total magnetic moments, thus impacting magnetic behavior, especially in CoB ions.[51] Exploring the electronic, magnetic, and sensing properties of these samples is intriguing, and theoretical studies provide valuable insights into the structures and properties of materials. First-principles calculations have predicted the activation of ferromagnetism in Co_3O_4, where oxygen vacancies notably influence spin states. Experimental and theoretical studies have demonstrated that creating these vacancies effectively triggers ferromagnetism, suggesting a promising pathway for manipulating the magnetic behavior of similar materials.[51,52]

Electrical Characterization. Figure 9 illustrates an $E-J$ curve displaying nonlinear behavior. With an increase in the applied current, the electric field reaches a maximum and subsequently decreases, indicating the presence of hysteretic

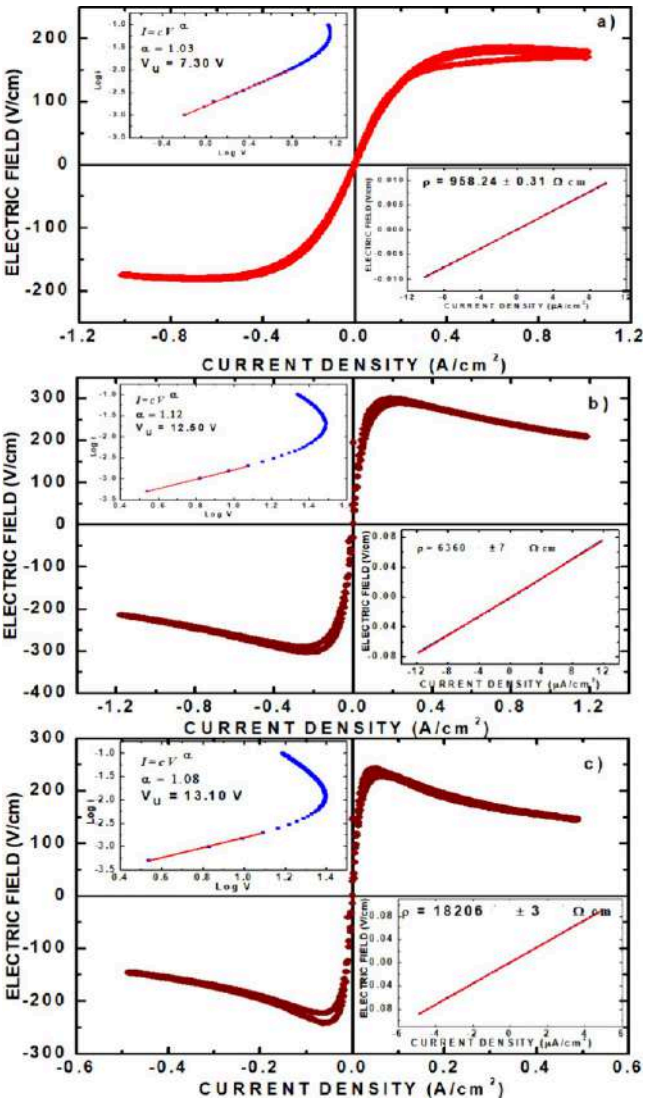

Figure 9. $E-J$ hysteresis curves obtained for (a) $Co_{3-x}Ni_xO_4$ synthesized using the sol–gel method, (b) $Co_{3-x}Ni_xO_4$-rGO synthesized using the sol–gel method, and (c) $Co_{3-x}Ni_xO_4$-rGO synthesized using the hydrothermal method at T = 292.5 K. The upper left inset shows the log(I) vs log(V) plot, and the lower right inset depicts the linear region of the hysteresis curve, method 2.

type in the system.[53] According to the literature, the nonlinear behavior of the electric field and current density can be attributed to the diversity in grain sizes and orientations, as well as the presence of Schottky barriers at the grain boundaries. These factors collectively contribute to the observed nonlinear electrical characteristics.[53] At low current densities, the current–voltage ($I-V$) curve exhibits a behavior that aligns with the figure of merit of the varistor, defined by

$$I = cV^{\alpha} \tag{1}$$

where $c = 1.78 \times 10^{-4}$ represents a constant, $\alpha = 1.03 \pm 0.01$ is the known varistor nonlinear coefficient, and V is the threshold voltage.[53]

In Figure 9a, the Co_3O_4 sample with 4% Ni prepared through the sol–gel method is presented. The hysteresis loop of the electric field indicates nonuniform current density for low and high currents. The open loop observed in the upper part may be attributed to Joule heating of the sample.[54] The

https://doi.org/10.1021/acsaelm.4c00638
ACS Appl. Electron. Mater. XXXX, XXX, XXX–XXX

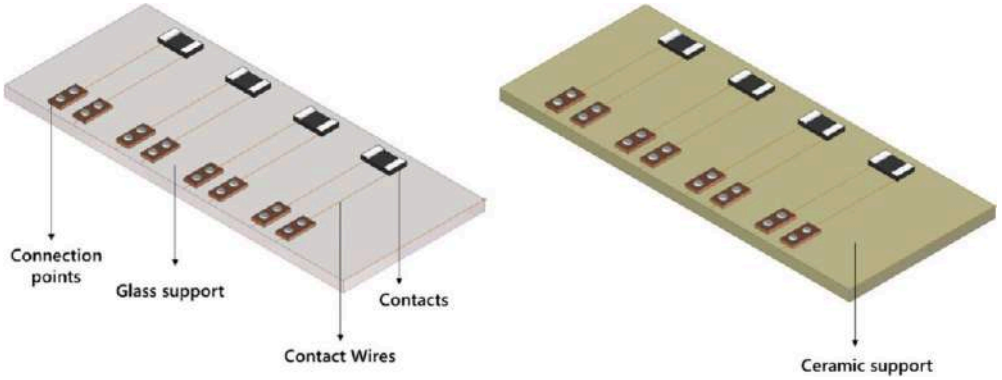

Figure 10. Diagram illustrating the sensor assembly, with a glass support used for method 1 and a ceramic support used for method 2.

left inset of Figure 9a displays a logarithmic plot of current ($\log(I)$) vs voltage ($\log(V)$) for the Co_3O_4 sample with 4% Ni at room temperature. The graph is linearly fitted in the only region to analyze the different linear or nonlinear regions, revealing distinct regions. For voltages below 7.3 V, a linear dependence is observed, suggesting that the transport follows Ohm's law. In the subsequent region, the conduction is space charge limited and trap-filled. In this region, electron traps, which are believed to be oxygen vacancies, gradually become filled with electrons, resulting in a gradual resistance.[55] According to Cuervo et al.,[53] the $I-V$ curve exhibits a behavior that conforms to that of a varistor, as seen in the equation of the graph in the left inset, where the voltage value is 7.3 V, respectively. In the right inset of Figure 9a, the linear region of the electric field vs current density was plotted. By linearizing the graph, the resistivity value of the sample was obtained, which is approximately 958 Ω·cm.

Figure 9b shows the electric field of the $Co_{3-x}Ni_xO_4$-rGO sample obtained by the sol−gel method and subsequently sintered and calcined. To gain a deeper insight into the charge transport phenomena, a comprehensive examination of the $I-V$ curve is conducted. By plotting the $I-V$ characteristic curve on a logarithmic scale, distinct slopes can be observed (Figure 9b). In the left inset, the initial region depicts a linear relationship between current and voltage, indicative of an ohmic behavior $I \propto V$, for values less than 1.1 V, and $I \propto V^2$ in the range 1.1 V < V < 1.5 V, corresponding to Child's law. However, in the subsequent region, a different slope is observed, suggesting the presence of trap controlled space charge limited current and the involvement of alternative transport mechanisms. In the second region, it is possible to calculate the effective mobility of carriers in the high-voltage region of the graph. The slope of this region can be utilized to evaluate the diffusion coefficient, with higher mobility, indicating a faster transport rate and potentially an increased number of charge carriers.[56]

Notably, a slight change at log V = 1.45 is observed, suggesting that the voltage reaches a level where the traps begin to fill. This phenomenon leads to the appearance of high-voltage square-law conduction, known as the trap-filled limit voltage. In the backward low-voltage region, as observed in Figure 9b and the left inset, a linear relationship between $\log(I)$ and $\log(V)$ with a slope of approximately −5 can be observed between log V = 1.5 and log V = 1.3. Interestingly, in the backward voltage region, $\log(I)-\log(V)$ exhibits a negative slope, nonlinearity parameter. However, no significant current drop is observed at the trap-filled limit voltage, indicating that the trap-filled state can be maintained even below that voltage. This behavior results in a distinct hysteresis and a bipolar resistive switching phenomenon with excellent resistance and sample retention.

It has been established that the resistive switching effect is primarily attributed to the presence of oxygen vacancies.[57] Oxygen vacancies alter spin structures in cobalt oxide, enhancing ferromagnetism and impacting magnetic and transport properties. Tension variation can further modify spin structures in Co_3O_4 films. These vacancies can also predominantly induce ferromagnetism, offering a novel pathway for transforming antiferromagnetic materials into ferromagnetic ones.[48,51] Additionally, the hysteresis behavior can be attributed to the trapping and unblocking of carriers from the trap sites.[58] The resistivity value for this particular sample is 6360 Ω·cm, which is higher than that for the sample shown in Figure 9a.

Figure 9c depicts the electrical behavior of the $Co_{3-x}Ni_xO_4$-rGO sample synthesized via the hydrothermal method. Similar to the sol−gel sample, the hysteresis curve exhibits a characteristic duckbill shape in the positive current region. However, the maximum current for the sol−gel hysteresis loop is 1.2 A/cm^2, while for the hydrothermal sample it is 0.5−1.2 A/cm^2. The hysteresis loop is not completely symmetric, with a slightly wider separation in the negative E region. When plotting $\log(I)$ vs $\log(V)$ in Figure 9c, a voltage of 13.1 V and a current density of 18206 Ω·cm are observed, compared to Figure 9a, which shows 12.5 V and a current density of 6360 Ω·cm.

In essence, Figure 9a exhibits varistor behavior with an α value close to 1 and a threshold voltage of 7.30 V. Figure 9b demonstrates thermistor behavior with α measuring 1.1 and a threshold voltage of 12.50 V. Lastly, Figure 9c thermistor displays a threshold voltage of 13.10 V.

The impact of very high and very low current densities on current sensing in a sensor can vary. In the case of very high current density, saturation of the sensor can occur. This means that the sensor reaches its maximum capacity to handle and accurately measure the high current flowing through it. Saturation can lead to distortion of the sensed current and affect the accuracy of the measurements.

On the other hand, very low current density can pose challenges in detecting and accurately measuring the current in the sensor. The sensitivity limitations and noise levels of the measurement system become more prominent when the current density is extremely low. It may result in difficulties in distinguishing the weak current signal from the background

https://doi.org/10.1021/acsaelm.4c00638
ACS Appl. Electron. Mater. XXXX, XXX, XXX−XXX

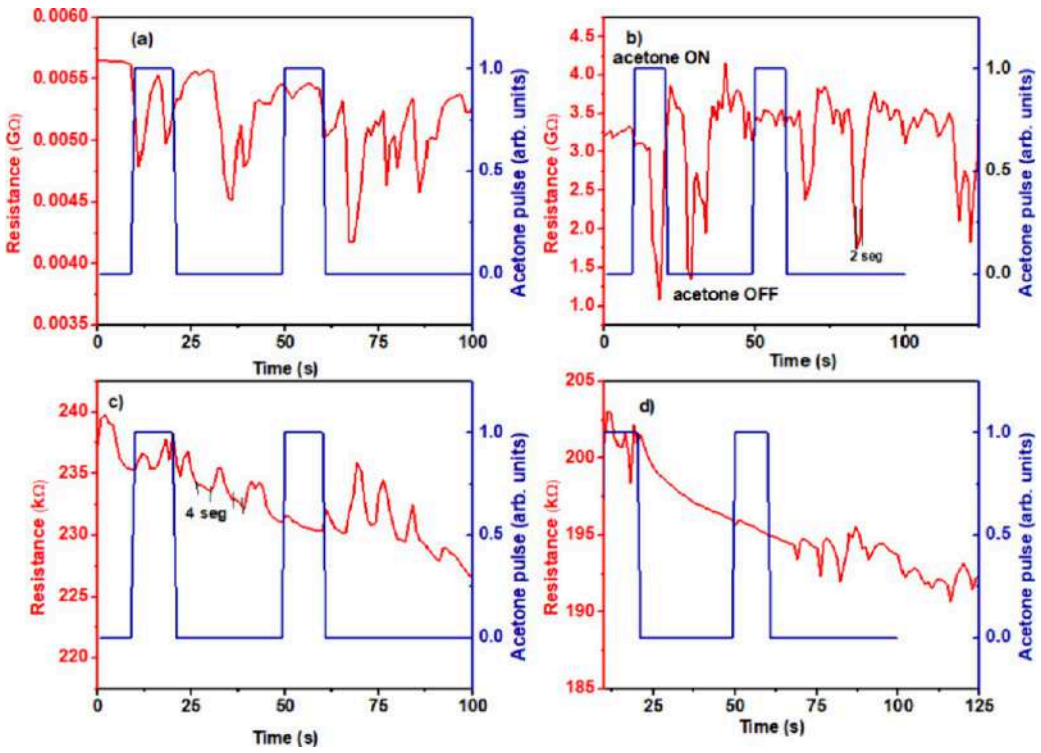

Figure 11. Method 1: Electrical resistance of Co_3O_4 nanoparticles after exposure to 1000 ppm acetone at room temperature for varying durations. (a, b) Samples prepared using the sol−gel method: $Co_{3-x}Ni_xO_4$ and $Co_{3-x}Ni_xO_4$-rGO, respectively. (c, d) Samples prepared using the hydrothermal method: $Co_{3-x}Ni_xO_4$- and $Co_{3-x}Ni_xO_4$-rGO, respectively.

noise, leading to less reliable measurements. Ferromagnetic materials, such as iron, nickel, and cobalt, exhibit electrical conductivity due to their electronic configuration, but not all conductive materials are ferromagnetic. Alterations in the crystal structure, such as oxygen vacancies, can induce ferromagnetic behavior and the formation of low-resistivity p-type semiconductors, thus affecting electrical conductivity and enhancing gas detection.

In the realm of integrated circuits, the material $Co_{3-x}Ni_xO_4$-rG could be utilized in manufacturing electronic components like sensors and transistors, leveraging its electrical conductivity and magnetic properties. Its compatibility with semiconductor processing techniques facilitates integration into existing chip architectures, while its catalytic properties offer opportunities for chemical detection and catalytic reactions. Additionally, as a detection element in detection platforms, this material could detect various environmental stimuli and enable real-time monitoring of environmental parameters or biomarkers in devices such as portable or microfluidic sensors.

Sensing Test for Acetone in the Samples for Method 1 and Method 2. Figure 10 illustrates the sensor assemblies specifically designed for conducting measurements using method 1. In this particular method, a paste was meticulously prepared by mixing isopropyl alcohol with the powdered samples, forming small pills. However, performing the measurements posed a significant challenge due to the delicate nature and fragility of these pellets.

In method 2, Figure 10, the powdered samples were compressed into pellets using a press and then subjected to a heat treatment at 1000 °C for 24 h. This approach facilitated the placement of contacts, as the resulting pellets were not fragile, enabling accurate sensing measurements to be performed on the samples. However, the disadvantage is that the material has been annealed expecting to return to the desired initial Co_3O_4 spinel phase.

Figure 11 illustrates the results obtained using method 1. In panels a and c of Figure 11, Co_3O_4 samples with a 4% Ni content are displayed, prepared through the sol−gel and hydrothermal methods, respectively. Panels b and d of Figure 11 exhibit the same samples but with the inclusion of rGO during the synthesis process, where panel b represents the sol−gel method and panel d corresponds to the hydrothermal method. Upon observing Figure 11, initially, the sensor samples may appear to exhibit unfavorable characteristics. The repeatability of acetone adsorption and desorption over time seems to be inconsistent, displaying nonuniform changes. Moreover, the presence of noise in the measurements hinders the identification of substantial variations.

Nevertheless, despite the identical composition of the samples prepared using different preparation methods, a remarkable disparity in resistance was observed. Specifically, the samples synthesized through the hydrothermal method exhibited diminished strength, in contrast to the sol−gel counterparts, which displayed relatively augmented strength. Given the p-type nature of Co_3O_4, the introduction of acetone is anticipated to elicit an elevation in resistance. According to the literature, previous studies on sensor response based on Co_3O_4 nanocubes at 500 ppm acetone have reported a higher response of 4.88 at 240 °C compared to Co_3O_4 nanospheres. The authors further demonstrate that the nanocubes exhibit a rapid response time of 2 s and a recovery process of 5 s to acetone, highlighting the significance of sample morphology.[59] In our study, however, we have employed a different synthesis method and evaluated the material's performance at room temperature.

https://doi.org/10.1021/acsaelm.4c00638
ACS Appl. Electron. Mater. XXXX, XXX, XXX−XXX

In previous studies, Co_3O_4 samples synthesized using the electrospray method demonstrated sensitivity to acetone at a working temperature of 200 °C. The response to 100 ppm acetone was reported as 8.61, with response and recovery times of 43 and 92 s, respectively.[60] It is worth noting that the response and recovery times obtained in our study were comparatively shorter, with times of 4 and 6 s, respectively. Upon observation of the results obtained in this method, it was evident that changes in the resistance were observed in the presence of acetone. However, the absorption and desorption mechanisms remained unclear due to the low-temperature conditions employed during the sensing test, which was conducted at room temperature. Therefore, it was deemed necessary to adjust the testing methodology. These sensors displayed p-type semiconductor behavior in the presence of acetone, with their resistance increasing upon exposure to the oxidizing gas. The response and recovery times were found to be very short. The sol−gel sample of $Co_{3-x}Ni_xO_4$-rGO showed a response of R = 2.5.

The electrical properties of the Co_3O_4 nanocomposites doped with nickel and rGO are observed in Table 1. According to the results, nickel doping indicates a resistivity in the average range of 30.35 Ω·cm. for the samples obtained by the hydrothermal technique, while nickel doping shows a decrease in resistivity when reduced graphene oxide is incorporated to the synthesized samples, i.e., an average value of 23.37 Ω·cm. It can be evidenced that the resistivity is lower for the samples with rGO addition.

Table 1. Calculation of Electrical Resistivity for $Co_{3-x}Ni_xO_4$-rGO and $Co_{3-x}Ni_xO_4$ Samples Obtained by the Hydrothermal and Sol−Gel Technique

	Resistivity (Ω·cm)			
	Hydrothermal		Sol−gel	
Temp (K)	Ni−Co_3O_4−rGO	Ni−Co_3O_4	Ni−Co_3O_4−rGO	Ni−Co_3O_4
291	23.30	31.72	51.73	98.58
292	23.55	31.35	50.02	96.50
293	23.42	30.74	49.17	95.04
294	23.06	30.26	48.43	93.57
295	22.81	29.89	47.70	91.62
296	22.45	29.28	47.09	89.91
297	22.20	29.04	46.36	88.26

rGO influenced the resistivity value, which is possibly related to the differences in the morphology of the samples. Furthermore, the presence of Ni^{2+} ions in the spinel structure enhances the conduction of hole mobility.[61] The obtained values depend on several factors, such as the amount and dispersion of cobalt oxide and graphene oxide nanoparticles, to make the nanocomposites electrically conductive.[62]

Panels a and b of Figure 12 demonstrate the sensitive response of the sol−gel method $Co_{3-x}Ni_xO_4$-rGO sample obtained using the second method, in which the pills were pressed and subsequently annealed at 1000 °C to obtain stronger and more manageable samples. The electrical resistance variations due to the pulsed addition of acetone in the sensors manufactured for the detection of C_3H_6O vapor with the $Co_{3-x}Ni_xO_4$-rGO can be observed in Figure 12. The graph illustrates the resistance change resulting from acetone adsorption and desorption. A notable alteration in electrical resistance is evident upon vapor−surface interaction for the samples, particularly pronounced at room temperature. Conversely, no significant changes were observed for samples synthesized via the hydrothermal method, hence their absence from the results. Only the sol−gel sample $Co_3-xNixO_4$-rGO is included. Moreover, at room temperature, the sensor's performance is suboptimal due to the slower desorption rate of vapors, hindering the clearance for subsequent acetone molecules upon vapor injection. The acetone detection behavior is attributed to the effective catalytic activity of Co^{2+} and Ni^{2+} ions within the spinel structure. In Figure 12b, the same sample as in Figure 12a was subjected to a temperature of 200 °C, resulting in clearer acetone absorption and desorption. Here, the resistance varies between 2720 and 2740 Ω, demonstrating the sensing behavior of the acetone.

According to the literature, the electrical conductivity of pure Co_3O_4 is low,[63] which limits the development of gas sensors with higher performance. By adding rGO to $Co_{3-x}Ni_xO_4$ samples, it was expected to improve the sensing performance. It is evident that graphene enhances the conductivity of the sample;[63] however, it does not contribute to the enhancement of active sites crucial for acetone detection. However, despite its significant surface area, the quantity of rGO utilized in this study is minimal; only a small amount (10 mg) was added during sample preparation. Consequently, the final surface area of the samples is not substantial solely due to the addition of rGO; other factors may also contribute to its size. Given that graphene primarily enhances carrier mobility, acetone oxidation occurs over the

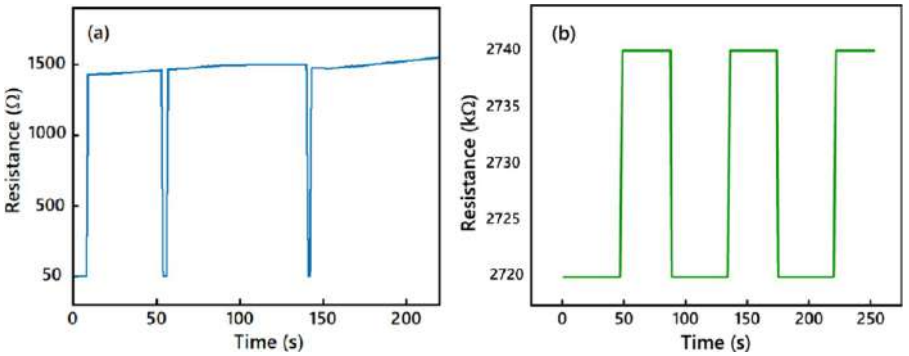

Figure 12. Time-dependent change in electrical resistance of a sensing device fabricated using the sol−gel technique with $Co_{3-x}Ni_xO_4$-rGO (x = 0.04) upon exposure to pulses of acetone vapor (a) at ambient temperature. (b) at temperature of 200 °C.

https://doi.org/10.1021/acsaelm.4c00638
ACS Appl. Electron. Mater. XXXX, XXX, XXX−XXX

Table 2. Summary of Some Acetone Gas Sensors Reported in the Literature

Sensing element	Synthesis approach	Operating temp (°C)	Response R_g/R type-p and R_a/R_g type- n	Ref
$YFeO_3$	Sol−gel method	128.1	12	64
WO_3	Electrospinning	200	10	65
$ZnFe_2O_4$	Sol−gel	300	18.5	66
$ZnFe_2O_4$	Solvothermal method	200	28	
Co_3O_4		240	4.9	67
$Co_{3-x}Ni_xO_4$-rGO				
method 1	Sol−gel	room temperature	2.5	this work
method 2	Sol−gel	200	1.1	this work

sample oxide. Therefore, optimizing the operating temperature becomes crucial to achieve a balance between rapid desorption and effective detection of C_3H_6O vapor. By carefully controlling the temperature conditions, it is possible to enhance the overall performance of the sensors and achieve improved sensitivity and response time for acetone detection.[64]

In previous studies, acetone detection at 1000 ppm was reported at 111 °C.[64] However, in our study, we observed a notable response at room temperature, although it did not reach the level of a strong response. Using this method, the sample exhibited a consistent and reliable response at high temperatures. Unlike the previous method, where resistance remained relatively stable over time in the presence of acetone, we observed significant changes in resistance at high temperatures following exposure to acetone. Additionally, at lower temperatures, the response was notably slower due to the absence of rapid desorption of acetone oxidation products. Reduced graphene oxide (rGO) plays a crucial role in enhancing the structure of Co_3O_4 by simultaneously improving electrical conductivity and increasing electroactive sites. This duality facilitates faster electron and ion transfer at the electrode−electrolyte interface, thereby improving the kinetics of electrochemical reactions. The high surface area of rGO enables strong adsorption capacity, with numerous surface defects and functional groups providing binding sites for acetone molecules. This results in prolonged saturation and slower desorption of acetone, which is critical for effective detection.

The interaction between gas and surface exposes Co^{2+} cations to acetone, leading to oxidation and reduction reactions, while grain boundaries enhance sensor performance in p-type materials. Response values are influenced by factors such as acetone concentration, temperature, morphology, and surface conditions, highlighting the importance of precise control in sensor design. Strategies to enhance selectivity toward acetone include temperature adjustment, metal decoration, porosity optimization, and refining sensor composition.[64] These characteristics, along with acetone concentration during absorption and desorption, are taken into account in Table 2.

Although method 1 exhibits a better sensing response to acetone, the absorption−desorption process of acetone in the sensing test is not well-defined. However, being a p-type material, its response is consistent, with low resistance in the absence of acetone that increases in the presence of acetone. In method 2, at a temperature higher than ambient, the sensing response is clear without any ambiguity. Nevertheless, it is lower compared to the previous case, and with the presence of acetone, the resistance increases.

Figure 13 illustrates the impact of acetone adsorption and reaction on electrical resistance of the sensor surface. The

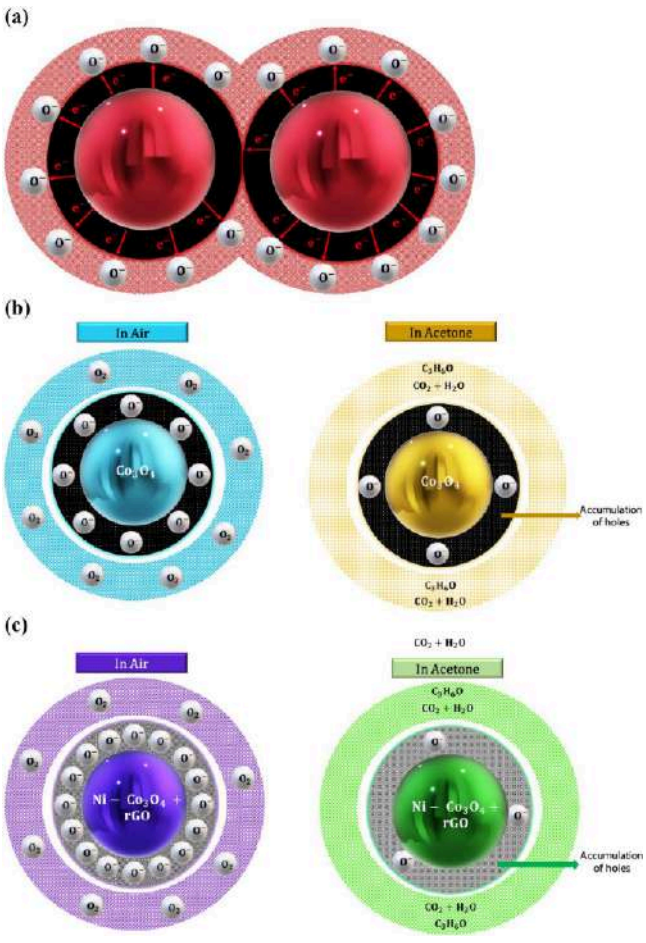

Figure 13. Electrical resistance of Co_3O_4 nanoparticles after exposure to 1000 ppm acetone at room temperature for varying durations. (a, b) Samples prepared using the sol−gel method: $Co_{3-x}Ni_xO_4$ and $Co_{3-x}Ni_xO_4$-rGO, respectively. (c) Samples prepared using the hydrothermal method: $Co_{3-x}Ni_xO_4$ and $Co_{3-x}Ni_xO_4$-rGO, respectively.

rGO-doped sample shows a more significant resistance change, indicating enhanced electrical resistivity modification. However, acetone detection performance at room temperature is compromised due to slow vapor desorption, resulting in delayed response time. The catalytic activity of Co^{2+} ions in cobalt oxide contributes to acetone detection.[24] The low electrical conductivity of pure Co_3O_4 hampers high-performance gas sensors, but rGO addition to $Co_{3-x}Ni_xO_4$improves carrier mobility.[68] Nonetheless, $Co_{3-x}Ni_xO_4$-rGO exhibits slowed acetone desorption at low temperatures, necessitating optimization of operating temperature for balanced response time and sensitivity. Gas sensing in doped cobalt oxide sensors

https://doi.org/10.1021/acsaelm.4c00638
ACS Appl. Electron. Mater. XXXX, XXX, XXX−XXX

involves acetone molecule adsorption, causing electrical resistance changes due to charge carrier modulation or surface reactions induced by acetone presence.[24]

Doping significantly enhances the gas response of p-type oxide semiconductors by modifying their electronic properties, leading to improved gas sensing capabilities.[69] Dopants introduce additional charge carriers or alter the band structure, thereby increasing sensitivity and selectivity to specific gases. For instance, in Ni-doped Co_3O_4, nickel dopant modifies the electronic structure, resulting in enhanced gas response, particularly to acetone and other target gases.

Chemical sensitization, involving noble metals or metal oxide catalysts on the semiconductor surface,[24] is commonly used to boost gas response in p-type oxide semiconductors. These catalysts enhance sensitivity by promoting surface reactions with the target gas, facilitating adsorption and desorption processes, and overall gas sensing performance. Optimizing particle size is crucial, as smaller sizes offer larger surface areas, improved gas accessibility, and heightened sensitivity to target gases. Although the exact relationship between particle size and gas response is still under investigation, reducing particle size shows promise for enhancing gas sensing capabilities.[24]

Gas sensing properties of p-type semiconductors,[24] including Ni-doped Co_3O_4, can be enhanced through various approaches such as morphological design, doping with elements like nickel, and integration of rGO. However, the presence of rGO with gas molecules like acetone may slow down the desorption process, impacting response time and sensitivity. Therefore, optimizing operating temperature is crucial for effective gas detection.[70] Chemical sensitization with noble metals or metal oxide catalysts enhances gas response through catalytic surface reactions, aiming to maximize surface area and improve sensitivity, selectivity, and response time in gas sensors. Ongoing research aims to advance p-type oxide semiconductor gas sensors for practical applications.

In Figure 13, the presence of oxygen ions (O_2^-) on the surface of the samples is evident, playing a significant role in surface reactions when acetone is introduced. Acetone acts as a reducing agent for the oxygen ions on the oxide surface, leading to their reduction and consequent changes in oxide resistance. This understanding of the interactions between organic compounds and inorganic surfaces has important implications for practical applications.

CONCLUSIONS

This study delved into the synthesis and characterization of $Co_{3-x}Ni_xO_4$-rGO samples, focusing on their electrical, magnetic, and acetone detection properties. Significant improvements were observed in samples incorporating 4% Ni and rGO via the sol−gel method, demonstrating altered magnetic behavior and enhanced electrical conductivity. The pivotal role of synthesis methods in shaping material properties was highlighted, with the sol−gel approach yielding particularly favorable results. Clearer results in acetone detection were obtained when samples underwent calcination postpressing, emphasizing their potential for sensor applications and underscoring the importance of synthesis techniques in tailoring properties for specific functionalities. Analysis confirmed the presence of the spinel phase in both materials, exhibiting distinct magnetic behaviors. Specifically, the sol−gel method produced materials displaying ferromagnetic behavior, thermistor-like semiconductor behavior, and high sensitivity to acetone, suggesting promising potential for multifunctional applications. Collectively, these findings underscore the versatility and potential of these materials in various electronic and sensing applications.

AUTHOR INFORMATION

Corresponding Author

Miryam Rincón Joya − *Departamento de Física, Universidad Nacional de Colombia Sede Bogotá, Bogotá 111321, Colombia;* orcid.org/0000-0002-4209-1698; Email: mrinconj@unal.edu.co

Authors

Leydi Julieta Cardenas F. − *Facultad de Ingeniería, Departamento de Ingeniería Mecánica y Mecatrónica, Universidad Nacional de Colombia Sede Bogotá, Bogotá 111321, Colombia; Departamento de Ingeniería Mecánica y Mecatrónica, Fundación Universidad de América, Bogotá 111711, Colombia*

Carlos Arturo Parra − *Grupo de Física de Materiales, Escuela de Física, Universidad Pedagógica y Tecnológica de Colombia, Tunja 150001, Colombia*

Javier Alonso Cuervo F. − *Grupo de Física de Materiales, Escuela de Física, Universidad Pedagógica y Tecnológica de Colombia, Tunja 150001, Colombia*

Adenilson José Chiquito − *NanOLaB, Departamento de Física, Universidade Federal de São Carlos (UFSCar), São Carlos 13565905, Brazil*

Luis Carlos Moreno A. − *Departamento de Química, Universidad Nacional de Colombia Sede Bogotá, Bogotá 111321, Colombia*

Julio Evelio Rodríguez − *Departamento de Física, Universidad Nacional de Colombia Sede Bogotá, Bogotá 111321, Colombia*

Complete contact information is available at: https://pubs.acs.org/10.1021/acsaelm.4c00638

Notes

The authors declare no competing financial interest.

ACKNOWLEDGMENTS

We thank Universidad Nacional de Colombia—Campus Bogotá, for Support for Research Projects, Artistic Creation and Innovation of the Universidad Nacional de Colombia-Bogotá-2020, Code 51055; QUIPU, NanOLAB UFSCAR Brazil, Universidad de América Foundation, for the time given to author L.J.C.F to write some parts and make some measurements; UPTC Tunja for the magnetic equipment; and Embrapa Brazil for FESEM measurements.

REFERENCES

(1) Gil-Barbarin, A.; Gutiérrez-Ortiz, J. I.; López-Fonseca, R.; de Rivas, B. Co_3O_4 hollow nanotubes for the catalytic oxidation of C_2-chlorinated VOCs. *J. Environ. Chem. Eng.* **2023**, *11*, 109841.

(2) Fan, J.; Yang, C.; Zhao, X.; Li, D.; Xiao, F.; Wu, R.; Wang, L. Enhanced gas sensing property of Co_3O_4 matrix nanocomposites with halloysite nanotubes toward triethylamine. *J. Mater. Res. Technol.* **2023**, *23*, 2491−2503.

(3) Chaudhuri, H.; Yun, Y. S. A critical review on the properties and energy storage applications of graphene oxide/layered double hydroxides and graphene oxide/MXenes. *J. Power Sources* **2023**, *564*, 232870−232870.

(4) Batool, M.; Hameed, A.; Nadeem, M. A. Recent developments on iron and nickel-based transition metal nitrides for overall water

splitting: A critical review. *Coord. Chem. Rev.* **2023**, *480*, 215029−215029.
(5) Tan, J.; Chen, X.; Shang, M.; Cui, J.; Li, D.; Yang, F.; Lin, X.; et al. N-doped biochar mediated peroxydisulfate activation for selective degradation of bisphenol A: The key role of potential difference-driven electron transfer mechanism. *Chem. Eng. J.* **2023**, *468*, 143476.
(6) Kumar, V. M.; Polaki, S. R.; Krishnan, R.; Sarguna, R. M.; Mathews, T. Binder-free vertical graphene nanosheets templated NiO petals for high-performance supercapacitor applications. *J. Alloys Compd.* **2023**, *931*, 167420−167420.
(7) Malafatti, J. O. D.; Moreira, A. J.; Paris, E. C.; Cardenas Flechas, L. J.; Pereira, O. A. P.; Rincon Joya, M. Evaluation of Ni-Doped Tricobalt Tetroxide with Reduced Graphene Oxide: Structural, Photocatalysis, and Antibacterial Response. *Catalysts* **2022**, *12* (10), 1199.
(8) Lakshmana Naik, R.; Bala Narsaiah, T. Hydrothermal synthesis and characterization of nanocrystalline zinc vanadate ($Zn_2V_2O_7$) on graphene oxide scaffolds. *Mater. Today: Proc.* **2023**, *72*, 268−273.
(9) Hussain, A.; Lakhan, M. N.; Soomro, I. A.; Ahmed, M.; Hanan, A.; Maitlo, A. A.; Zehra, I.; Liu, J.; Wang, J. Preparation of reduced graphene oxide decorated two-dimensional WSe_2 nanosheet sensor for efficient detection of ethanol gas. *Physica E (Amsterdam, Neth.)* **2023**, *147*, 115574.
(10) Basu, A. K.; Chauhan, P. S.; Awasthi, M.; Bhattacharya, S. α -Fe_2O_3 loaded rGO nanosheets based fast response/recovery CO gas sensor at room temperature. *Appl. Surf. Sci.* **2019**, *465*, 56−66.
(11) Bai, H.; Guo, H.; Wang, J.; Dong, Y.; Liu, B.; Xie, Z.; Guo, F.; Chen, D.; Zhang, R.; Zheng, Y. A room-temperature NO_2 gas sensor based on CuO nanoflakes modified with rGO nanosheets. *Sens. Actuators, B* **2021**, *337*, 129783.
(12) Bhuvaneswari, C.; Ganesh Babu, S. Nanoarchitecture and surface engineering strategy for the construction of 3D hierarchical CuS-rGO/g-C_3N_4 nanostructure: An ultrasensitive and highly selective electrochemical sensor for the detection of furazolidone drug. *J. Electroanal. Chem.* **2022**, *907*, 116080.
(13) Hwang, K.; Ahn, J.; Cho, I.; Kang, K.; Kim, K.; Choi, J.; Polychronopoulou, K.; Park, I. Microporous elastomer filter coated with metal organic frameworks for improved selectivity and stability of metal oxide gas sensors. *ACS Appl. Mater. Interfaces* **2020**, *12*, 13338−13347.
(14) Achary, L. S. K.; Kumar, A.; Barik, B.; Nayak, P. S.; Tripathy, N.; Kar, J. P.; Dash, P. Reduced graphene oxide-$CuFe_2O_4$ nanocomposite: A highly sensitive room temperature NH_3 gas sensor. *Sens. Actuators, B* **2018**, *272*, 100−109.
(15) Zou, Y.; Wang, Q.; Xiang, C.; Tang, C.; Chu, H.; Qiu, S.; Yan, E.; Xu, F.; Sun, L. Doping composite of polyaniline and reduced graphene oxide with palladium nanoparticles for room-temperature hydrogen-gas sensing. *Int. J. Hydrogen Energy* **2016**, *41*, 5396−5404.
(16) Tiwari, D. C.; Atri, P.; Sharma, R. Sensitive detection of ammonia by reduced graphene oxide/polypyrrole nanocomposites. *Synth. Met.* **2015**, *203*, 228−234.
(17) Meng, F.; Zheng, H.; Chang, Y.; Zhao, Y.; Li, M.; Wang, C.; Sun, Y.; Liu, J. One-step synthesis of Au/SnO_2/RGO nanocomposites and their VOC sensing properties. *IEEE Trans. Nanotechnol.* **2018**, *17*, 212−219.
(18) Ngo, Y.-L. T.; Hoa, L. T.; Chung, J. S.; Hur, S. H. Multi-dimensional Ag/NiO/reduced graphene oxide nanostructures for a highly sensitive non-enzymatic glucose sensor. *J. Alloys Compd.* **2017**, *712*, 742−751.
(19) Yang, Y.; Jiang, M.; Cao, K.; Wu, M.; Zhao, C.; Li, H.; Hong, C. An electrochemical immunosensor for CEA detection based on Au-Ag/rGO@ PDA nanocomposites as integrated double signal amplification strategy. *Microchem. J.* **2019**, *151*, 104223.
(20) Zhu, P.; Li, S.; Zhao, C.; Zhang, Y.; Yu, J. 3D synergistical rGO/Eu (TPyP)(Pc) hybrid aerogel for high-performance NO2 gas sensor with enhanced immunity to humidity. *J. Hazard Mater.* **2020**, *384*, 121426−121426.
(21) Wang, L.; Wu, A.; Wei, G. Graphene-based aptasensors: from molecule-interface interactions to sensor design and biomedical diagnostics. *Analyst* **2018**, *143*, 1526−1543.
(22) Manikandan, V. S.; Adhikari, B.; Chen, A. Nanomaterial based electrochemical sensors for the safety and quality control of food and beverages. *Analyst* **2018**, *143*, 4537−4554.
(23) Wilson, A. D.; Baietto, M. Applications and Advances in Electronic-Nose Technologies. *Sensors* **2009**, *9*, 5099−5148.
(24) Kim, H. J.; Lee, J. H. ighly sensitive and selective gas sensors using p-type oxide semiconductors: Overview. *Sens. Actuators, B* **2014**, *192*, 607−627.
(25) Kim, T.-H.; Yoon, J.-W.; Kang, Y. C.; Abdel-Hady, F.; Wazzan, A.A.; Lee, J.-H. A strategy for ultrasensitive and selective detection of methylamine using p-type Cr_2O_3: Morphological design of sensing materials, control of charge carrier concentrations, and configurational tuning of Au catalysts. *Sens. Actuators, B* **2017**, *240*, 1049−1057.
(26) Hashtroudi, H.; Yu, A.; Juodkazis, S.; Shafiei, M. Ultra-Sensitive Photo-Induced Hydrogen Gas Sensor Based on Two-Dimensional CeO2-Pd-PDA/rGO Heterojunction Nanocomposite. *Nanomaterials* **2022**, *12*, 1628.
(27) Li, L.; Xu, Q.; Zhang, Y.; Li, J.; Fang, J.; Dai, Y.; Cheng, X.; You, Y.; Li, X. Low Ni-doped Co_3O_4 porous nanoplates for enhanced hydrogen and oxygen evolution reaction. *J. Alloys Compd.* **2020**, *823*, 153750.
(28) Cardenas Flechas, L. J.; Raba Paez, A. M.; Rincon Joya, M. Synthesis and evaluation of nickel doped Co_3O_4 produced through hydrothermal technique. *DYNA* **2020**, *87*, 184−191.
(29) Min, S.; Zhao, C.; Chen, G.; Qian, X. One-pot hydrothermal synthesis of reduced graphene oxide/Ni $(OH)_2$ films on nickel foam for high performance supercapacitors. *Electrochim. Acta* **2014**, *115*, 155−164.
(30) Pakdel, A.; Bando, Y.; Golberg, D. Nano boron nitride flatland. *Chem. Soc. Rev.* **2014**, *43*, 934−959.
(31) Zhang, J.; Zeng, D.; Zhu, Q.; Wu, J.; Huang, Q.; Xie, C. Effect of nickel vacancies on the room-temperature NO_2 sensing properties of mesoporous NiO nanosheets. *J. Phys. Chem. C* **2016**, *120*, 3936−3945.
(32) Li, Y.; Wang, S.; Hao, P.; Tian, J.; Cui, H.; Wang, X. Soft-templated formation of double-shelled ZnO hollow microspheres for acetone gas sensing at low concentration/near room temperature. *Sens. Actuators, B* **2018**, *273*, 751−759.
(33) Jang, K. B.; Park, K. R.; Mo, C. B.; Kim, S.; Jeon, J.; Lim, S. c.; Ahn, C.; Han, H.; Kim, D.; Lee, S. H.; Kim, K. M.; Mhin, S. Synthetic control of the surface area in nickel cobalt oxide for glucose detection via additive-assisted wet chemical method. *Sci. Rep.* **2022**, *12*, 19546.
(34) Cardenas-Flechas, L.; Freire, P. T. C.; Paris, E. C.; Moreno, L. C.; Joya, M. R. Temperature-induced structural phase transformation in samples of Co_3O_4 and $Co_{3-x}Ni_xO_4$ for CoO. *Materialia* **2021**, *18*, 101155.
(35) Cardenas F, L. J.; Chimenos, J. M.; Moreno A, L. C.; Paris, E. C.; Joya, M. R. Enhancing Co_3O_4 nanoparticles: Investigating the impact of nickel doping and high-temperature annealing on $NiCo_2O_4$/CoO heterostructures. *AIMS Mater. Sci.* **2023**, *10*, 1090−1104.
(36) Zhu, H. T.; Luo, J.; Liang, J. K.; Rao, G. H.; Li, J. B.; Zhang, J. Y.; Du, Z. M. Synthesis and magnetic properties of antiferromagnetic Co_3O_4 nanoparticles. *Phys Rev. B: Condens. Matter Matter Phys.* **2008**, *403*, 3141−3145.
(37) Shepit, M.; Paidi, V. K.; Roberts, C. A.; van Lierop, J. Competing ferro- and antiferromagnetic exchange drives shape-selective nanomagnetism. *Sci. Rep.* **2020**, *10*, 20990.
(38) Taghizadeh, F. Fabrication and Investigation of the Magnetic Properties of Co and Co_3O_4 Nanoparticles. *Opt. Photon. J.* **2016**, *6*, 62−68.
(39) Svanidze, E.; Wang, J. K.; Besara, T.; Liu, L.; Huang, Q.; Siegrist, T.; Frandsen, B.; Lynn, J. W.; Nevidomskyy, A. H.; Gamża, M. B.; Aronson, M. C.; Uemura, Y. J.; Morosan, E. An itinerant antiferromagnetic metal without magnetic constituents. *Nat. Commun.* **2015**, *6*, 7701.

https://doi.org/10.1021/acsaelm.4c00638
ACS Appl. Electron. Mater. XXXX, XXX, XXX−XXX

(40) Matharu, A. S.; Grover, C.; Komitov, L.; Andersson, G. Ferro-ferri- and antiferro-electric behaviour in a bent-shaped mesogen. *J. Mater. Chem.* **2000**, *10*, 1303−1310.
(41) Hu, B.; He, W.; Ye, J.; Tang, J.; Zhang, Y.-S.; Ahmad, S. S.; Zhang, X.-Q.; Cheng, Z.-H. Determination of magnetic anisotropy constants and domain wall pinning energy of Fe/MgO(001) ultrathin film by anisotropic magnetoresistance. *Sci. Rep.* **2015**, *5*, 14114.
(42) Yadagiri, K.; Nithya, R.; Sharma, S.; Satya, A. T. Modification of low temperature magnetic interactions in $Dy_{1-x}Eu_xMnO_3$. *RSC Adv.* **2018**, *8*, 13537−13545.
(43) Larumbe, S.; Gómez-Polo, C.; Pérez-Landazábal, J. I.; García-Prieto, A.; Alonso, J.; Fdez-Gubieda, M.; Cordero, D.; Gómez, J. Ni doped Fe_3O_4 magnetic nanoparticles. *J. Nanosci Nanotechnol* **2012**, *12*, 2652.
(44) Ichiyanagi, Y.; Kimishima, Y.; Yamada, S. Magnetic study on Co_3O_4 nanoparticles. *J. Magn. Magn. Mater.* **2004**, *272-276*, E1245−E1246.
(45) Singh, V.; Kosa, M.; Majhi, K.; Major, D. T. Putting DFT to the Test: A First-Principles Study of Electronic, Magnetic, and Optical Properties of Co_3O_4. *J. Chem. Theory Comput.* **2015**, *11*, 64−72.
(46) Giri, N.; Biswas, B. S.; Sengupta, P.; Ray, R. Exchange bias and magnetic memory effect in hole doped $Nd_{0.78}Sr_{0.22}CoO_3$ nanoparticles. *RSC Adv.* **2022**, *12*, 26470−26475.
(47) Taghizadeh, F. Fabrication and Investigation of the Magnetic Properties of Co and Co_3O_4 Nanoparticles. *Opt. Photonics J.* **2016**, *6*, 62−68.
(48) Ramos Ramon, J. A.; Ortiz-Quinonez, J. L.; Ray, A.; Das, S.; Pal, U. Inducing Superparamagnetism and High Magnetization in Nickel Cobaltite ($Ni_xCo_{3-x}O_4$) Spinel Nanoparticles by Controlling Ni Mole Fraction and Cation Distribution. *J. Phys. Chem. C* **2020**, *124*, 18264−18274.
(49) Ghobadi, N.; Bahiraie, H.; Kazazzi, M. Effect of Ni Substitution on Optical Transitions and Magnetic Behavior of Mesoporous ($Ni_xCo_{3-x}O_4$) ($0 \leq x \leq 1$) Thin Films Prepared by Electrophoretic Deposition. *J. Electron. Mater.* **2021**, *50*, 987−991.
(50) Mulinari, T. A.; La Porta, F. A.; Andrés, J.; Cilense, M.; Varela, J. A.; Longo, E. Microwave-hydrothermal synthesis of single-crystalline Co_3O_4 spinel nanocubes. *CrystEngComm* **2013**, *15* (37), 7443.
(51) Magray, M. A.; Ikram, M.; Najim, M. Impact of oxygen vacancies to control the magnetic and electronic properties of the La_2CoMnO_6 system. *J. Magn. Magn. Mater.* **2021**, *529*, 167857.
(52) Wang, P.; Jin, C.; Li, P.; Zheng, D.X.; Gong, J.L.; Bai, H.L. Oxygen vacancies induced ferromagnetic behaviors in Co_3O_4_δ: An experimental and first-principles study. *Thin Solid Films* **2018**, *660*, 287−293.
(53) Farfan, J. A. C.; Lara, J. P. B.; Vargas, C. A. P.; Tellez, D. A. L.; Roa-Rojas, J. Structural Characteristics and Electric and Magnetic Features of the $Nd_{2.68}Sr_{1.32}Mn_{1.2}Ti_{1.32}Fe_{1.48}O_{12}$ Ferromagnetic Semiconductor. *J. Low Temp. Phys.* **2021**, *202*, 128−144.
(54) Wang, F.; Zou, T.; Liu, Y.; Yan, L.-Q.; Sun, Y. Extrinsic and intrinsic nonlinear current-voltage characteristics in charge ordered oxides. *J. Appl. Phys.* **2012**, *111*, 033703.
(55) Liu, C. F.; Tang, X.; Wang, L. Q.; Tang, H.; Jiang, Y. P.; Liu, Q. X.; Li, W. H.; Tang, Z. Resistive Switching Characteristics of HfO_2 Thin Films on Mica Substrates Prepared by Sol-Gel Process. *Nanomaterials* **2019**, *9*, 1124.
(56) Dutta, B.; Dey, A.; Naskar, K.; Maity, S.; Ahmed, F.; Islam, S.; Sinha, C.; Ghosh, P.; Ray, P. P.; Mir, M. H. Two isostructural linear coordination polymers: the size of the metal ion impacts the electrical conductivity. *New J. Chem.* **2018**, *42*, 10309.
(57) Hu, C.; Wang, Q.; Bai, S.; Xu, M.; He, D.; Lyu, D.; Qi, J. The effect of oxygen vacancy on switching mechanism of ZnO resistive switching memory. *Appl. Phys. Lett.* **2017**, *110*, 073501.
(58) Fu, Y. J.; Xia, F. J.; Jia, Y. L.; Jia, C. J.; Li, J. Y.; Dai, X. H.; Fu, G. S.; Zhu, B. Y.; Liu, B. T. Bipolar resistive switching behavior of $La_{0.5}Sr_{0.5}CoO_{3-\sigma}$ films for nonvolatile memory applications. *Appl. Phys. Lett.* **2014**, *104*, 223505.
(59) Zhou, T.; Zhang, T.; Deng, J.; Zhang, R.; Lou, Z.; Wang, L. P-type Co_3O_4 nanomaterials-based gas sensor: Preparation and acetone sensing performance. *Sens. Actuators, B* **2017**, *242*, 369−377.
(60) Fan, X.; Xu, Y.; Ma, C.; He, W. In-situ growth of Co_3O_4 nanoparticles based on electrospray for an acetone gas sensor. *J. Alloys Compd.* **2021**, *854*, 157234.
(61) Liu, Y.; Fergus, J. W.; Cruz, C. D. Electrical properties, cation distributions, and thermal expansion of manganese cobalt chromite spinel oxides. *J. Am. Ceram. Soc.* **2013**, *96*, 1841−1846.
(62) Iranshahi, S.; Mosivand, S. Cobalt/graphene oxide nanocomposites: Electro-synthesis, structural, magnetic, and electrical properties. *Ceram. Int.* **2022**, *48*, 12240−12254.
(63) He, Y.; Zhang, N.; Wu, F.; Xu, F.; Liu, Y.; Gao, J. Graphene oxide foams and their excellent adsorption ability for acetone gas. *Mater. Res. Bull.* **2013**, *48*, 3553−3558.
(64) Amiri, V.; Roshan, H.; Mirzaei, A.; Neri, G.; Ayesh, A. Nanostructured Metal Oxide-Based Acetone Gas Sensors: A Review. *Sensors* **2020**, *20*, 3096.
(65) Ghosh, P.; Manikandan, M.; Sen, S.; Devi, P. S. Some interesting insights into the acetone sensing characteristics of monoclinic WO_3. *Mater. Adv.* **2023**, *4*, 1146−1160.
(66) Zhang, G.; Li, C.; Cheng, F.; Chen, J. ZnFe2O4 tubes: Synthesis and application to gas sensors with high sensitivity and low-energy consumption. *Sens. Actuators, B* **2007**, *120*, 403−410.
(67) Zhou, X.; Wang, B.; Sun, H.; Wang, C.; Sun, P.; Li, X.; Hu, X.; Lu, G. Template-free synthesis of hierarchical $ZnFe_2O_4$ yolk-shell microspheres for high-sensitivity acetone sensors. *Nanoscale* **2016**, *8*, 5446−5453.
(68) Zhou, T.; Chen, S.; Wang, X.; Xie, C.; Zeng, D. Catalytic Activation of Cobalt Doping Sites in ZIF-71-Coated ZnO Nanorod Arrays for Enhancing Gas-Sensing Performance to Acetone. *ACS Appl. Mater. Interfaces* **2020**, *12*, 48948−48956.
(69) Tong, B.; Meng, G.; Deng, Z.; Gao, J.; Liu, H.; Dai, T.; Wang, S.; Shao, J.; Tao, R.; Kong, F.; Tong, W.; Luo, X.; Fang, X. Sc-doped NiO nanoflowers sensor with rich oxygen vacancy defects for enhancing VOCs sensing performances. *J. Alloys Compd.* **2021**, *851*, 155760.
(70) da Silva, L. F.; Catto, A. C.; Avansi, W.; Cavalcante, L. S.; Mastelaro, V. R.; Andres, J.; Aguir, K.; Longo, E. Acetone gas sensor based on a-Ag_2WO_4 nanorods obtained via a microwave-assisted hydrothermal route. *J. Alloys Compd.* **2016**, *683*, 186−190.

https://doi.org/10.1021/acsaelm.4c00638
ACS Appl. Electron. Mater. XXXX, XXX, XXX−XXX